

Scanning Fabry–Perot Interferometer of the 6-m SAO RAS Telescope

A.V. Moiseev

Special Astrophysical Observatory, Russian Academy of Sciences, Nizhnij Arkhyz, 369167 Russia

the date of receipt and acceptance should be inserted later

Abstract. The scanning Fabry–Perot interferometer (FPI) — is the oldest method of optical 3D spectroscopy. It is still in use because of the high spectral resolution it provides over a large field of view. The history of the application of this method for the study of extended objects (nebulae and galaxies) and the technique of data reduction and analysis are discussed. The paper focuses on the performing observations with the scanning FPI on the 6-m telescope of the Special Astrophysical Observatory of the Russian Academy of Sciences (SAO RAS). The instrument is currently used as a part of the SCORPIO-2 multimode focal reducer. The results of studies of various galactic and extragalactic objects with the scanning FPI on the 6-m telescope—star-forming regions and young stellar objects, spiral, ring, dwarf and interacting galaxies, ionization cones of active galactic nuclei, galactic winds, etc. are briefly discussed. Further prospects for research with the scanning FPI of the SAO RAS are discussed.

Key words. techniques: interferometric—techniques: image processing—techniques: imaging spectroscopy—instrumentation: interferometers

1. Introduction

Fabry–Perot interferometers (FPI) based on the principles that were first described by Fabry & Perot (1901) have been used for more than one hundred years to study motions of ionized gas in various astrophysical objects. Successful measurements of the distribution of line-of-sight velocities in the Orion nebula were performed using an interferometer made of two parallel mirrors shortly before World War I (Buisson et al., 1914). After a short pause this technique of the study of gaseous nebulae was revived in Marseille Observatory (Courtès, 1960); it became increasingly popular and improved progressively. In Soviet astronomy such observations were introduced mainly by P. V. Schcheglov (Sheglov, 1963). The FPIs developed by Shcheglov were used to perform extensive studies of the kinematics of supernova remnants and other emission nebulae on the 48- and 125-cm telescopes of the Crimea station of Sternberg Astronomical Institute of Moscow State University (Lozinskaya, 1969, 1973).

The result of observations with a FPI with a fixed distance between the plates (the “Fabry–Perot etalon”) is an image—an interferogram where spatial and spectral information is mixed, so that each point (x, y) in the image plane corresponds to a wavelength λ varying with distance from the optical axis (Fig. 1). In such a frame the Doppler

velocities can only be measured in separate regions of the nebula that satisfy the condition of maximum interference:

$$n\lambda = 2l\mu \cos \theta, \quad (1)$$

where l and μ are the gap and refraction index of the medium between the interferometer plates and θ is the beam incidence angle converted into the radius of the interference ring. The idea of a scanning interferometer consists in varying the right-hand part of formula (1). Although the possibility of mechanically moving the plates in a FPI was implemented as early as in the 1920s, observations were first performed using more reliable schemes that involved tilting the interferometer with respect to the line of sight or varying the pressure and hence the μ value of the medium where the etalon is placed. For a detailed description of the history of the development of various technical solutions, which ended in the use of piezoelectric scanning systems allowing controlled variation of l see Atherton (1995).

In 1969 observations of the motions of ionized gas in the $H\alpha$ line in the M51 galaxy were made on the 2.1-m telescope of Kitt Peak Observatory using a FPI scanned by varying pressure. Photographic plates scanned on a microdensitometer after exposure were used as detectors. This technique made it possible to reconstruct a set of emission-line spectra filling the image of the galaxy considered (Tully, 1974). Similar principles were used in “Galaxymetr” device employed to reconstruct gas veloc-

Send offprint requests to: Alexei Moiseev e-mail: moisav@gmail.com

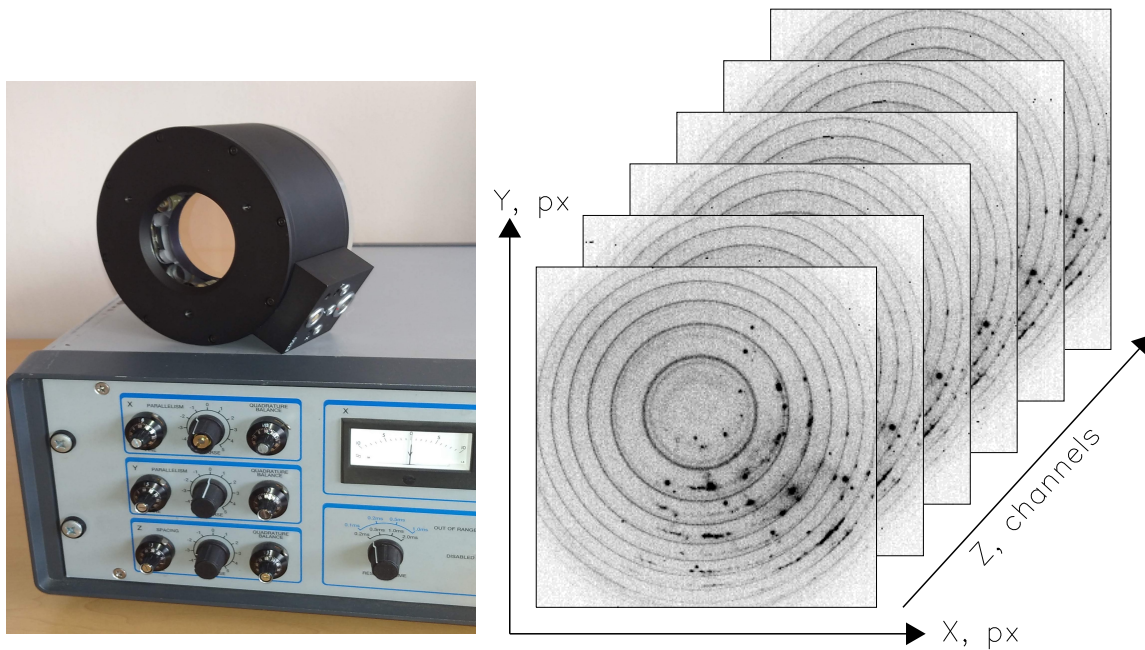


Fig. 1. Left: ET50-FS-100 scanning FPI and CS100 controller used in observations on the 6-m telescope. Right: the initial data cube of “raw” interferograms acquired with SCORPIO-2 in H α line in February 2020; every sixth channel is shown. The uniformly bright rings represent night-sky airglow emission lines in different interference orders. The footprints of H II regions of the NGC 4535 galaxy can be seen.

ity fields in galaxies of various types (de Vaucouleurs & Pence, 1980).

These observations marked the beginning of panoramic (aka 3D) spectroscopy operating with the concept of “data cube” in the (x, y, λ) space. Here wavelengths λ (or Doppler velocities of a certain line) are the third (spectral) coordinate. Spectrographs can be subdivided into two main types by the method used to register the data cube (Monnet, 1995): those with simultaneous and sequential recording. Integral-field spectrographs (IFS) simultaneously record spectra from all spatial elements made in the form of an array of microlenses (Bacon et al., 1995), fiber bundle (Arribas et al., 1991), or a system of image slicer mirrors (Weitzel et al., 1996; Bacon et al., 2014). The best solution for spectrophotometric tasks proved to be a combination of microlenses and optical fibers (Courtes, 1982), which was first implemented in the MPFS spectrograph attached to the 6-m telescope of the Special Astrophysical Observatory of the Russian Academy of Sciences (SAO RAS) (Afanasiev et al., 1990b, 2001).

In spectrographs with sequential registration (FPIs and Fourier spectrographs) the third coordinate in the data cube appears as a result of additional exposures. In the case of a scanning FPI we are dealing with a set of interferograms acquired by varying the optical path $l\mu$ between the mirrors (Fig. 1). This solution allows achieving a large field of view combined with high spectral resolution, albeit in a narrow wavelength range. High spectral resolution is important for studying the gas velocity dispersion

from the broadening of emission lines in star-forming regions (Roy et al., 1986; Melnick et al., 1987).

Before the end of the 20th century the number of nebulae and galaxies studied using scanning FPIs was perhaps greater than the number of such objects observed using all other 3D spectroscopy methods. Let us point out the contribution of such systems as TAURUS (Taylor & Atherton, 1980), TAURUS-2 (Gordon et al., 2000), HIFI (Bland & Tully, 1989), and CIGALE (Boulesteix et al., 1984) operated on telescopes with diameters greater than 3 meters. Unfortunately, listing all devices and the results obtained is beyond the scope of this review. Let us just point out two important trends. First, the need to perform scanning under changing atmospheric conditions makes it efficient to use the strategy of repeated acquisition of interferograms with short exposures. Image Photon Counting Systems (IPCS), which in other areas have been superseded by CCDs with higher quantum efficiency, proved to perform well in that case. Second, scanning FPIs are currently much less popular compared to IFS. This is due both to higher versatility of the latter in observations in small ($< 1'$) fields of view and to the fact that the data acquired with FPI are often considered to be too “complicated and peculiar” from the point of view of the analysis and interpretation compared to classical spectroscopy¹. However, in their dedicated fields, such as the study of the kinematics and morphology of ionized gas, FPIs can be used to carry out mass homogeneous surveys. For ex-

¹ Here we do not discuss the instruments used with solar telescopes, where FPIs play a very important role.

Table 1. Systems with a scanning FPI on large and medium-sized telescopes

Telescope/Device	FOV, ′	\mathcal{R}	Detector	References
10.4-m GTC/OSIRIS	8	400–800 ¹	CCD	González et al. (2014)
10-m SALT/RSS	8	1 500	CCD	Mitchell et al. (2015)
6.5-m Magellan/MMTF	27	400–1 000 ¹	CCD	Veilleux et al. (2010)
6-m BTA/SCORPIO-2	6.1	500 ¹ , 4 000, 16 000	CCD	Afanasiev & Moiseev (2011)
4.2-m WHT/GHαFaS	4.7	15 000	IPCS	Hernandez et al. (2008)
4.1-m SOAR/SAM-FP	3	11 000	CCD	Mendes de Oliveira et al. (2017)
2.5-m SAI MSU/MaNGaL	5.6	500 ¹	CCD	Moiseev et al. (2020)
2.1-m OAN/PUMA	10	16 000	CCD	Rosado et al. (1995)

¹ tunable filter mode

ample, the GHASP project, which resulted in the study of the kinematics of 203 spiral and irregular galaxies (Epinat et al., 2008).

Table 1 lists the characteristics of current systems based on scanning FPIs operating on medium- and large-diameter telescopes with results published in recent years: name of the telescope and the instrument, field of view (FOV), spectral resolution $\mathcal{R} = \lambda/\delta\lambda$, detector type, and a reference to the description. Unfortunately, the current list contains fewer items than a similar list compiled more than 30 years ago (Bland & Tully, 1989) despite the fact that a number of telescopes listed in Table 1 were not yet constructed at the time. Moreover, according to the information provided on the websites of the respective observatories some of the instruments listed in the table were either under reconstruction (the system on SALT telescope) or decommissioned (MMTF) at the time of writing this review. One third of the list represent FPIs with low spectral resolution operating in the tunable filters mode with a 10–20 Å bandwidth: the corresponding data cube usually contains just a few channels (images taken in the emission line and in the nearby continuum).

As is evident from Table 1, the 6-m Big Telescope Alt-Azimuth (BTA SAO RAS) remains the world’s largest telescope used for regular 3D spectroscopic observations with a scanning FPI of high ($\mathcal{R} > 10\,000$) spectral resolution. The telescope is also equipped with low ($\mathcal{R} < 1\,000$) and intermediate-resolution ($\mathcal{R} \sim 5\,000$) interferometers. It is not surprising that such a wide range of capabilities combined with more than four-decades long history of the use of this method on the 6-m telescope contributed to performing many interesting studies of the interstellar medium both in the Milky Way and beyond. Below we discuss the history of the succession of generations of instruments using scanning FPIs on the 6-m telescope and the characteristics of this method when used in SCORPIO-2 device (Section 2). Then, after discussing the data reduction and analysis (Section 3), we consider concrete published results concerning the study of the kinematics of galaxies of various types (Section 4) and of the influence of star formation on the interstellar medium on scale lengths ranging from several parsecs to ten kiloparsecs (Section 5). In Conclusions (Section 6) we discuss further prospects of using this method on our telescope.

2. History of the FPIs on the SAO RAS 6-m telescope

The idea of using a focus-shortening facility (focal reducer) was proposed and implemented by Courtes back in the 1950–1960s (Courtès, 1960). The focal reducer provides optimal match between the angular size of star images and detector elements and decreases the equivalent focal ratio, which is important for the study of extended objects. The optics of the focal reducer allows it to be mounted in the parallel beam between the collimator and the camera of the dispersing element (grisms or FPI), thereby converting the reducer into a multimode spectrograph. It was a team from Marseilles Observatory in cooperation with colleagues from SAO RAS that began studying the motions of ionized gas in galaxies on the 6-m telescope using an FPI equipped with a guest reducer providing an equivalent focal ratio of $F/1.5$ – $F/1.6$ in the primary focus. The first interferograms of the NGC 925 galaxy were acquired directly on photographic plates (October 28, 1978), during observations in September 1979 a two-stage image RSA tube was mounted in front of the photo cassette. The acquired data were used to construct the H α line-of-sight velocity field. Despite averaging of observed velocities over rather large $14'' \times 14''$ “pixels” it was possible not only to reconstruct the rotation curve of the galaxy, but also estimate perturbations in the gas motions induced by the spiral density wave (Marcelin et al., 1982). In October 1980 and January 1981 the first interferograms of emission lines of ionized gas in M 33, NGC 925, and VV 551 were acquired with Marseilles’ IPCS “COLIBRI” (“Comptage linéaire de Brilliance”, Boulesteix et al., 1982). The velocity field of the NGC 2403 spiral galaxy and its rotation curve were inferred from the four interferograms (Marcelin et al., 1983).

In 1985 a focal reducer for interferometric observations providing a focal ratio of $F/2.2$ was made at SAO RAS based on commercial camera lenses. A Queensgate Instruments Ltd. (UK) piezoelectrically-scanned FPI was acquired within the framework of a joint project with CNRS (France). The detector employed was a 512×512 KVANT (Afanasiev et al., 1987) photon counter with a scale of $0.46''/\text{px}$. This system described in detail by Dodonov et al. (1995) was usually referred to as CIGALE (“Cinématique des Galaxies”) named after its prototype,

the automated focal reducer with a scanning FPI and IPCS made by the Marseilles team for the 3.6-m CFHT telescope (Boulesteix et al., 1984). The first publication based on the results obtained from observations made with CIGALE on the 6-m telescope appears to be the study of the kinematics of the active galaxy Mrk 1040 (Afanasiev et al., 1990a). In 1997 the KVANT photon counter was replaced by a low readout noise $1k \times 1k$ CCD.

Within the framework of the same Franco-Soviet co-operation observations were organized using a scanning FPI at the 2.6-m telescope of Byurakan Astrophysical Observatory (BAO) in Armenia (Boulesteix et al., 1987). Initially, the French colleagues brought the original CIGALE system from CFHT, which was also earlier used with the 6-m telescope. Later, a new reducer was assembled for the 2.6-m telescope using a CCD operating in half-obscured mode. Note that both the FPIs and the set of band-splitting filters often travelled from one observatory to another to different sides of the Caucasus Mountain Range. From 1991 it also meant travelling between different countries. In the early 2000s, under an agreement the colleagues, the high-resolution interferometer and filters were transferred to the SAO RAS to conduct joint studies (see Section 5).

Despite such shortcomings as poor seeing at the edge of the field of view, low transmission of the optics, and the lack of automation, the focal reducer described above was used with the 6-m telescope for over ten years, until it became necessary to fundamentally upgrade it. In 1999 the work began on the development of a new SCORPIO focal reducer under the supervision of V. L. Afanasiev with the participation of the author of this review (Afanasiev & Moiseev, 2005). The instrument saw first light on September 21, 2000.

SCORPIO² was a multimode instrument where the FPI was just one of the options for observations along with direct imaging, grism spectroscopy, and spectropolarimetry. The equivalent focal ratio in the primary focus of the 6-m telescope was F/2.6 (the initial focal ratio before the replacement of the optics in 2003 was F/2.9). The detector employed before 2003 was a 1024×1024 TK1024 CCD, which was later replaced with a EEV 42-40 2048×2048 CCD. This resulted in a minor change of the field of view (from $5'.4$ to $6'.1$), because the geometric pixel size of the above CCDs was equal to 24 and $13.5 \mu m$, respectively. Observations with the FPI are usually performed in the binning mode in order to reduce the readout time and readout noise and increase the signal-to-noise ratio. In the case of EEV 42-40 4×4 or 2×2 px² binning was mostly applied, which corresponds to a scale of $0''.72$ and $0''.36$, respectively.

The universal layout of the instrument, its high quantum efficiency, and the fact that it allows fast change of observing programs depending on the current atmo-

Table 2. Parameters of scanning FPIs in SCORPIO-2 (for $\lambda = 6563 \text{ \AA}$)

	IFP20	IFP186	IFP751	IFP501
n	20	188	751	501
$\Delta\lambda, \text{ \AA}$	328	34.9	8.7	13.1
$\delta\lambda, \text{ \AA}$	13	1.7	0.44	0.80
F	25	21	20	16
n_z	–	40	40	36

spheric conditions resulted in about 50% of all nights on the 6-m telescope since 2006 being allocated to observations performed with SCORPIO (Afanasiev & Moiseev, 2011). However, the instrument has become quite obsolete over more than ten years of its operation, and this is combined with ever mounting needs and requests of the observers. That is why a new focal reducer, SCORPIO-2, was developed at SAO RAS under the supervision of V. L. Afanasiev. The first observations with the new instrument were carried out on June 22, 2010.

Since 2013 FPI observations on the 6-m telescope are performed only with SCORPIO-2. The instrument has the same equivalent focal ratio, and uses a 4612×2048 E2V 42-90 CCD with a pixel size of $13.5 \mu m$ as a detector since 2020, resulting in the same angle image scale as in the case of old SCORPIO. Since 2020 observations are performed with a new camera based on a 4096×2048 E2V 261-84 CCD with a physical pixel size of $15 \mu m$, resulting in a scale of $0''.8$ and $0''.4$ in the 4×4 and 2×2 readout modes, respectively. With both “rectangular” CCDs the full detector format is used only in observations in spectral modes, whereas in the FPI and direct imaging modes a 2048×2048 px square fragment is cut out.

All the above nitrogen-cooled CCD cameras were made at the Advanced Design Laboratory of SAO RAS as described in Ardilanov et al. (2020).

2.1. FPI Kit at SAO RAS

The list of ET50-FS-100 type scanning piezoelectric interferometers (clear aperture 50 mm) available for observations with SCORPIO-2 is provided in Table 2. Here n is the interference order at the center of the field of view for observations in rest-frame H α line; $\Delta\lambda = \lambda/n$ is the distance between the neighboring orders that determines the free wavelength interval; $\delta\lambda$, FWHM of the instrumental contour, which determines the spectral resolution; $F = \Delta\lambda/\delta\lambda$, the finesse, which primarily depends on the properties of reflecting coatings of the interferometer mirrors; n_z , the number of channels into which the free wavelength interval is partitioned, it determines the dimension of the data cube along the “spectral” coordinate. The lowest-order interferometer (IFP20) is used for observations in the tunable filter mode when only a small part of $\Delta\lambda$ is scanned, and therefore the parameter n_z is unimportant in that case. More details about this type of observations can be found in Moiseev et al. (2020).

² After the reconstruction performed in 2019 the instrument continued to be operated with the 6-m telescope under the name of SCORPIO-1.

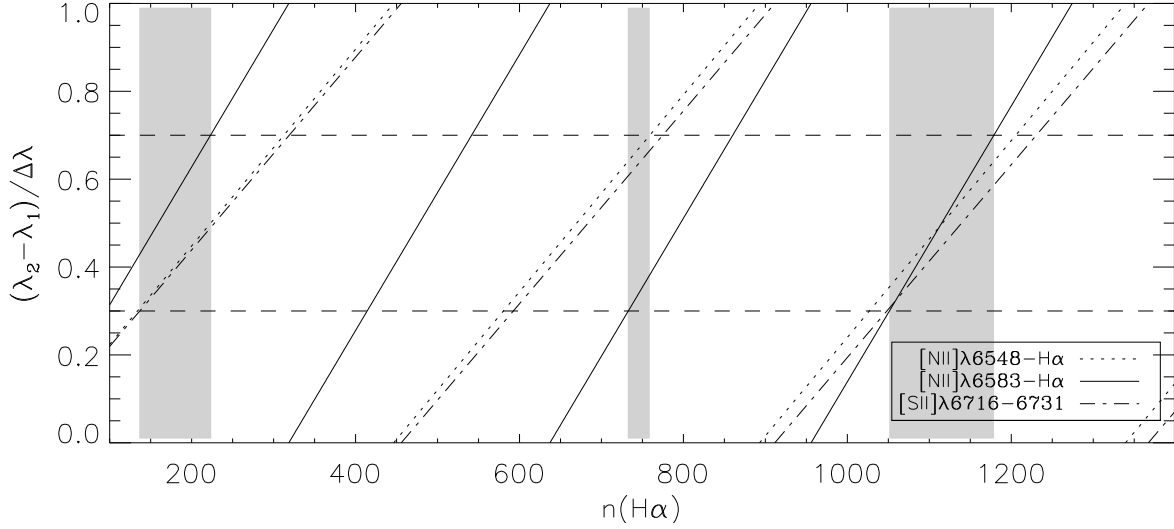


Fig. 2. Dependence of the fractional distance between close lines on interference order (at the $H\alpha$ wavelength). The lines of different types show different variants of λ_1 – λ_2 pairs. The horizontal dashes indicate the domain of “good separation”, where the observed distance between the lines is within $(0.5 \pm 0.2)\Delta\lambda$. The gray-filled regions corresponds to the range of n , where this condition is fulfilled.

The interferometers IFP751, IFP186, and IFP20 were manufactured for SAO RAS by the UK company IC Optical Systems Ltd³ (former Queensgate Instruments) in 2009, 2012, and 2016, respectively. The IFP501 interferometer was used for observations with CIGALE system back in the 1980–1990s, and later for observations with SCORPIO. It is still in working condition, however IFP751 should be preferred for most of the tasks performed with high spectral resolution. The old interferometer operating in $n(H\alpha)=235$ and used in CIGALE and SCORPIO is currently in nonoperable state and is was replaced with IFP186.

The need to work with different n is due to two factors. First, like in the case of classic spectroscopy, low resolution allows achieving higher signal-to-noise ratio in each spectral channel with the same exposure, i.e., makes it possible to observe fainter objects than with high resolution. However, in the cases where the redshifted line of the object is located at practically the same wavelength as night-sky emission lines, higher resolution may become necessary. Second, given the technical challenge of achieving $F > 30$, high interference orders n are needed to achieve high spectral resolution $\delta\lambda$:

$$\mathcal{R} = \frac{\lambda}{\delta\lambda} = \frac{\lambda F}{\Delta\lambda} = nF.$$

This, in turn, reduces the distance $\Delta\lambda$ between the neighboring orders, thereby restricting the velocity interval available for unambiguous determination of this quantity. Thus IFP751 produces for $H\alpha$ an instrumental profile with $\text{FWHM} \approx 20 \text{ km s}^{-1}$, which allows studying the distribution of velocity dispersion and multicomponent structure of emission lines in star-forming regions (Section 5).

Note that the width of the operating range of observed velocities is equal to $\Delta v \approx 390 \text{ km s}^{-1}$, which is less than the scatter of velocities in interacting or active galaxies. Therefore a line at wavelength λ cannot be distinguished from a component with Doppler shift $\lambda + \Delta\lambda$ based on interferometer data alone. In some cases this can be achieved using additional information, e.g., obtained from long-slit spectroscopy. At the same time, observations with IFP186 ($\Delta v \approx 1600 \text{ km s}^{-1}$) allow practically unambiguous interpretation of such kinematic components, but this is achieved at the expense of the loss of resolution ($\text{FWHM} \approx 77 \text{ km s}^{-1}$).

Yet another problem in observations with a scanning FPI arises in the “red” wavelength interval, where the wavelength difference between closely located bright lines of ionized gas is as small as about 15 \AA , which is less than $\Delta\lambda$ for $n > 400$. This is the case for $H\alpha + [\text{N II}]\lambda 6548, 6583$ and $[\text{S II}]\lambda 6716, 6731$ line systems. The narrow-band filters with $\text{FWHM} = 12\text{--}25 \text{ \AA}$ described in the next section cannot completely suppress the emission from neighboring lines and therefore it is important that their wavelength difference would not be equal to a multiple of $\Delta\lambda$. The optimum line separation is when their wavelengths λ_1 and λ_2 differ by half-order, i.e.:

$$|\lambda_2 - \lambda_1| = (0.5 + k)\Delta\lambda = (0.5 + k)\frac{\lambda_1}{n}, \quad (2)$$

where $k = 0, 1, 2, \dots$. Fig. 2 illustrates the problem of choosing n for optimal separation of all the above close pairs of spectral lines, which correspond to different slanting lines in the plot. It is evidently impossible to achieve the ideal fulfillment of condition (2) for all pairs, but a softer criterion—requiring for the lines to be separated within $(0.3\text{--}0.7)\Delta\lambda$ can be satisfied by several intervals of interference order values n . The first one corresponds to

³ <https://www.icopticalsystems.com/>

$k = 0$ and $n \approx 150\text{--}200$. The parameters of IFP186 were chosen based on this criterion. The next “optimum” domain with $n \approx 750$ corresponds to the IFP751 interferometer. In the third domain with $n \approx 1100$ practically all line pairs satisfy the “hard” criterion (2). Such interferometers ($n = 1051, 1353$) were used to perform the first observations on the 6-m telescope of SAO RAS (Marcelin et al., 1982). However, in that case $\Delta v < 300 \text{ km s}^{-1}$ in the $\text{H}\alpha$ line, which is too small for many tasks of extragalactic astronomy. Moreover, given that the width of interference rings decreases with \mathcal{R} , care must be used to ensure bona fide resolution of rings across the entire field of view (i.e. $\text{FWHM} > 2 \text{ px}$).

It goes without saying that the best solution would be using a single FPI allowing the gap between the plates to be accurately varied from 10 to 500 μm , which would cover the entire required range of n . Unfortunately, this is impossible to achieve with commercially available piezoelectric interferometers, and laboratory developments have not yet been completed (Marcelin et al., 2008).

2.2. Narrow-Band Filters

According to formula (1), in the case of non-monochromatic radiation, each pixel of the interferogram contains a signal at wavelengths corresponding to different interference orders, so that $n\lambda = \text{const}$. When considering the data cube, this means “packing” light with different wavelengths within a narrow spectral interval (see our Fig. 3 as well as Fig. 2 in the paper Daigle et al., 2006). It is therefore necessary to isolate the spectral interval under study in order to reduce stray illumination from the object and from the night sky lines. The ideal solution would be to use a narrow-band filter with a rectangular transmission profile with a width of $\Delta\lambda$ wide centered on the required emission line. This ideal could be closely approximated by a system of two FPIs with widely differing interference orders tuned so that in the case of scanning their transmission peaks would always coincide at the desired wavelength. The spectral resolution is set by a large-gap interferometer ($n \approx 200\text{--}1000$), and the free spectral interval is determined by an interferometer with $n = 10\text{--}30$. The latter gives $\Delta\lambda = 200\text{--}600 \text{ \AA}$ for the $\text{H}\alpha$ line. Isolating such a wide band is not a problem for modern intermediate-band interference filters and is practically realized in the case of the FPI operating in the tunable filter mode (Veilleux et al., 2010; Moiseev et al., 2020). Systems based on dual FPIs have long been efficiently operated on solar telescopes (see, for example Kentischer et al., 1998) and have even been used to observe bright comets (Morgenthaler et al., 2001).

Unfortunately, the author do not know about efficiently working systems for night observations using a dual scanning FPI, although the corresponding projects have been repeatedly announced (Rangwala et al., 2008; Marcelin et al., 2008). A possible partial exception is

the WHAM instrument used to study the diffuse gas of both the Milky Way (Haffner et al., 2003) and the Large Magellanic Cloud (Ciampa et al., 2021). High spectral resolution and sensitivity are achieved using two fixed-gap Fabry–Perot etalons, but the low angular resolution (1°) prevents its use for studying most galaxies and nebulae.

A simple and common solution to isolate the required part of the spectrum is to use narrow bandwidth filters $\text{FWHM} \approx \Delta\lambda$. However, in this case several factors limit the efficiency of observations. First, a set of filters with overlapping transmission curves centered on the corresponding systemic velocities is needed to isolate the emission lines of galaxies in a given redshift range. Second, manufacturing interference filters of sufficiently large diameter, with a bandwidth of a few nanometers and peak transmission no lower than 70–80% is quite a challenging technical task. Such filters are available from only a few manufacturers in the world and are quite expensive. The cost of a set of 10–15 such filters is close to that of scanning FPI with the same light diameter. Third, the transmission profile of such filters is usually close to Gaussian. This can lead to significant transmission variations within the operating wavelength range, as well as to light from neighboring orders of interference in the wings of the filter transmission profile. Note also that the peak transmission wavelength of narrow-band filters varies significantly (in FWHM units) with the ambient temperature.

The observers often consider the lines of the object “coming” from neighboring interference orders as a parasitic pollution. There are papers whose authors mistook the $[\text{N II}]$ emission from other orders as the second subsystem of ionized gas in the $\text{H}\alpha$ line. On the other hand, if the condition (2) was fulfilled when choosing the interferometer parameters and the emission lines in the object studied are narrow enough for their confident separation, it becomes possible to investigate the gas kinematics using the data for two emission lines. In the case of $\text{H}\alpha + [\text{N II}]$ we are dealing with lines with different excitation mechanism. It becomes possible to study effects related with shocks with nitrogen line emission intensified relative to the Balmer lines. Therefore, the brightness and the line-of-sight velocity distribution of these lines may differ. Figure 3 shows an example of simultaneous observations of the nitrogen and hydrogen lines in the NGC 1084 galaxy (see also Section 5). This mode of observation can also be useful for studying ionized gas in early-type galaxies where $\text{H}\alpha$ line in the central regions is hidden in a contrast underlying absorption of the stellar population spectrum, whereas $[\text{N II}]$ continues to be visible. At the same time, the $\text{H}\alpha$ line is much brighter than $[\text{N II}]$ in the H II regions at the periphery of the stellar disk. An example of simultaneous reconstruction of the line-of-sight velocity fields in these lines for the NGC 7742 galaxy can be found in Sil’chenko & Moiseev (2006).

The filters available in SCORPIO-2 allow observing objects with line-of-sight velocities ranging from -200 to $13\,500 \text{ km s}^{-1}$ in the $\text{H}\alpha$ line, to about $6\,000 \text{ km s}^{-1}$ in the $[\text{S II}]\lambda 6717$ line and to about $17\,000 \text{ km s}^{-1}$ in the

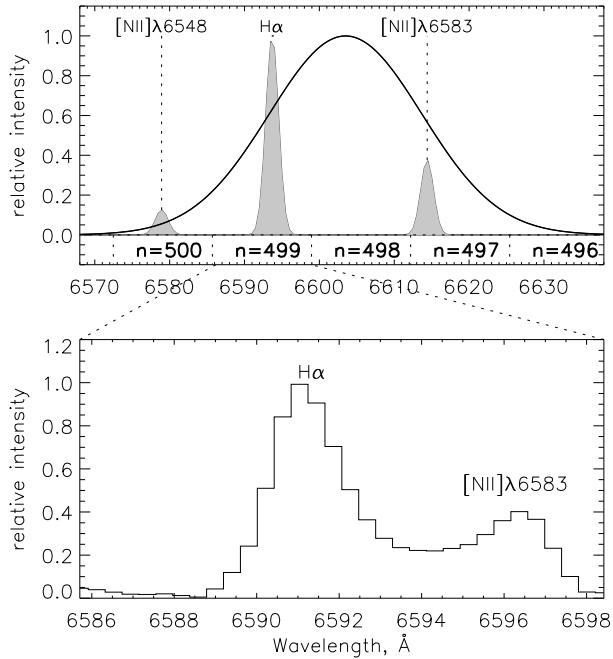


Fig. 3. Lines of ionized gas in the NGC 1084 galaxy (Moiseev, 2000). Top: the relative location of the H α + [N II] lines (the gray filled area) and the narrow-band filter (the thick line) in the wavelength scale. The numbers indicate interference orders ($n = \dots$) separated by $\Delta\lambda$ gaps. Bottom: spectrum observed with the FPI.

[O III] $\lambda 5007$ line. Of course, other lines can also be observed with this filter set. Finkelman et al. (2011) reconstructed the polar ring galaxy velocity field at $z = 0.06$ ($V_{\text{sys}} \approx 18\,000 \text{ km s}^{-1}$) in the H β line. The current list of filters is available in the web page of the instrument⁴; one can also download from this site the latest version of the program for choice the optimum filter for the given line, redshift and air temperature.

This filter kit has been collected at SAO RAS over many years as a result of various cooperative programs and grants. The collection started with several filters for observations near the H α line, which was provided by colleagues from Byurakan Astrophysical Observatory and manufactured by Barr Associates Inc. (USA) at the request of Marseilles Observatory. This set was extended with filters manufactured for SAO RAS by the Institute for Precision Instrument Engineering (IPIE, Moscow). Later, filters manufactured by Andover Corporation (USA) were purchased from different sources. Unfortunately, after 15 years of operation use the filters manufactured by the IPIE were partially degraded. Now these filters are almost all replaced with analogs from Andover Corporation. Most filters have a clear aperture of 50 mm (2 inches)—a common standard among many manufacturers. Unfortunately, this size is not sufficient to cover the field of view diagonally, so there is vignetting in the frame corners, which is noticeable in the interfero-

grams in Fig. 1. A good tradeoff between size and cost are the 50 mm wide square filters from Custom Scientific, Inc. (USA). They almost completely cover the SCORPIO-2 field of view.

Based on experience in separating close lines from neighboring orders, our team at SAO RAS currently prefers filters with $\text{FWHM} \approx 30 \text{ Å}$, which are twice wider than those with which we began FPI observations on the 6-m telescope. One of the advantages of these filters is their near-rectangular transmission curve in contrast to the Gaussian profile of the more narrow-band filters.

3. Data reduction and analysis

Primary reduction of the data acquired with the scanning FPI includes both the standard procedures for CCD frame reduction (bias subtraction, flatfielding, and cosmic-ray hit removal) and specific procedures: channel-by-channel photometric correction and wavelength calibration taking into account the phase shift. A sufficiently detailed description of the basic principles and algorithms can be found in several works (Bland & Tully, 1989; Gordon et al., 2000; Moiseev, 2002). A detailed description of the IFPWD software package used for processing SCORPIO FPI can be found in Moiseev & Egorov (2008), where the technique of glare subtraction are discussed and the accuracy of velocity and velocity-dispersion measurements with different FPIs is evaluated. Additional procedures used to improve the accuracy of the wavelength scale by using the “A-cube” are described in Moiseev (2015).

3.1. Sky Background Subtraction

Let us now consider in detail the procedure for subtracting the night-sky background in the IFPWD package, where some important modifications have been made that were not described in the papers published in 2002–2015. In observations with the photon-counting system, variations in the brightness of the sky background (emission lines of the Earth’s upper atmosphere, scattered light from the Moon, etc.) are averaged into the final cube by repeat scanning cycles with short (10–30 s) integration times of individual interferograms. This allows the sky background to be subtracted from the wavelength-calibrated spectra by averaging over areas free of the emission from the object, like it is usually done in classical spectroscopy. Such a principle was used in the ADHOC software suite (J. Boulesteix) developed for processing CIGALE data. Modern modifications of this algorithm are described Daigle et al. (2006). However, in the case of CCD observations, several minutes long exposures are needed because of the non-zero noise and readout times. Here one can no longer neglect background variations within the resulting cube; it must be subtracted from each frame even before wavelength calibration by averaging the sky emission over the azimuthal angle φ in concentric rings (Moiseev, 2002). It is important to accurately determine the center of the system of interference rings from the sky lines. The IFPWD package

⁴ <https://www.sao.ru/hq/lsfvo/devices/scorpio-2/>

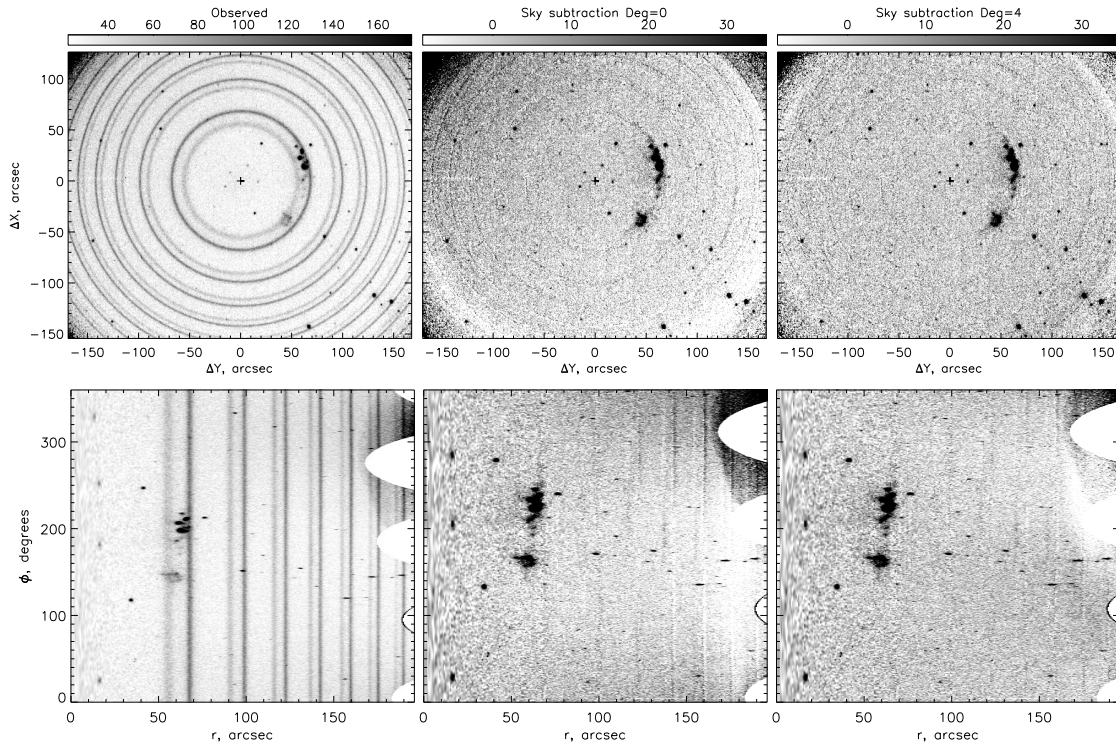


Fig. 4. Subtraction of night-sky lines in the case of observations of the UGC 4115 galaxy. The top row shows the observed frames and the bottom row shows the same frames in polar coordinate system (r, ϕ). Left to right: the initial interferogram, subtraction of sky emission in the case of simple averaging (zero-order polynomial) and by fitting the night-sky lines by a fourth-order polynomial.

provides an automatic mode to search for the center by the minimizing the deviation of the averaged background profile from the observed profile.

In the case of observations of low surface brightness objects deviations of the sky background pattern from a simple concentric model become significant because of the variations of the instrumental contour across the field due to optical aberrations, FPI settings, detector tilt, etc. The deviations increase towards the edge of the field of view, where the interference rings are thinner and the background model should be as accurate as possible. Previously, we used averaging the background over individual sectors by the angle φ . This technique works well for objects fitting into a small field of view (Moiseev & Egorov, 2008). A better result can be obtained by constructing the background model in the polar coordinate system. Here the background intensity at a given radius r can be represented as a simple function $I_r(\varphi)$. Figure 4 shows examples of the description of this function by a polynomial, where the zero degree corresponds to simple azimuthal averaging $I_r(\varphi) = \text{const}$. As is evident from the figure, the fourth-degree polynomial provides a better result of background subtraction.

Currently, given the increasing number of tasks involving observations of objects that occupy the entire field of view of the instrument (construction of mosaics for nearby galaxies, etc.), we are working on modelling the intensity distribution of the sky emission lines with the variations

of the instrumental contour taken into account. A similar approach was used, for example, for the MUSE FPI (Streicher et al., 2011; Soto et al., 2016) data reduction.

3.2. Representation and Analysis of the Data Cube

The problem of optimal visualization and presentation of data cubes, both in the process of analysis and in publications, is common to all methods of 3D spectroscopy. Despite the well-known progress in the dynamic visualization of “3D” spectral data (Punzo et al., 2015), it is more convenient to operate with two-dimensional maps and graphs for interpreting the data and explaining the results to the colleagues. The specificity of the FPI data cubes (large field of view and small extent along the spectral coordinate) allows visualization methods to be used similar to those employed in the analysis of radio observations of molecular and atomic gas. Figure 5 demonstrates this with the example of the dwarf galaxy NGC 428 studied with the FPI on SCORPIO-2 (Egorova et al., 2019). The channel maps reveal the spatial arrangement of regions with different kinematics. The “position–velocity” (P-V) diagram focuses on the line-of-sight velocities and the shape of the spectral lines along a given direction. The brightness distribution map in the $H\alpha$ emission line is useful for highlighting individual H II regions whose profiles can be viewed individually. The line-of-sight velocity distribution (velocity field) can be described by some model

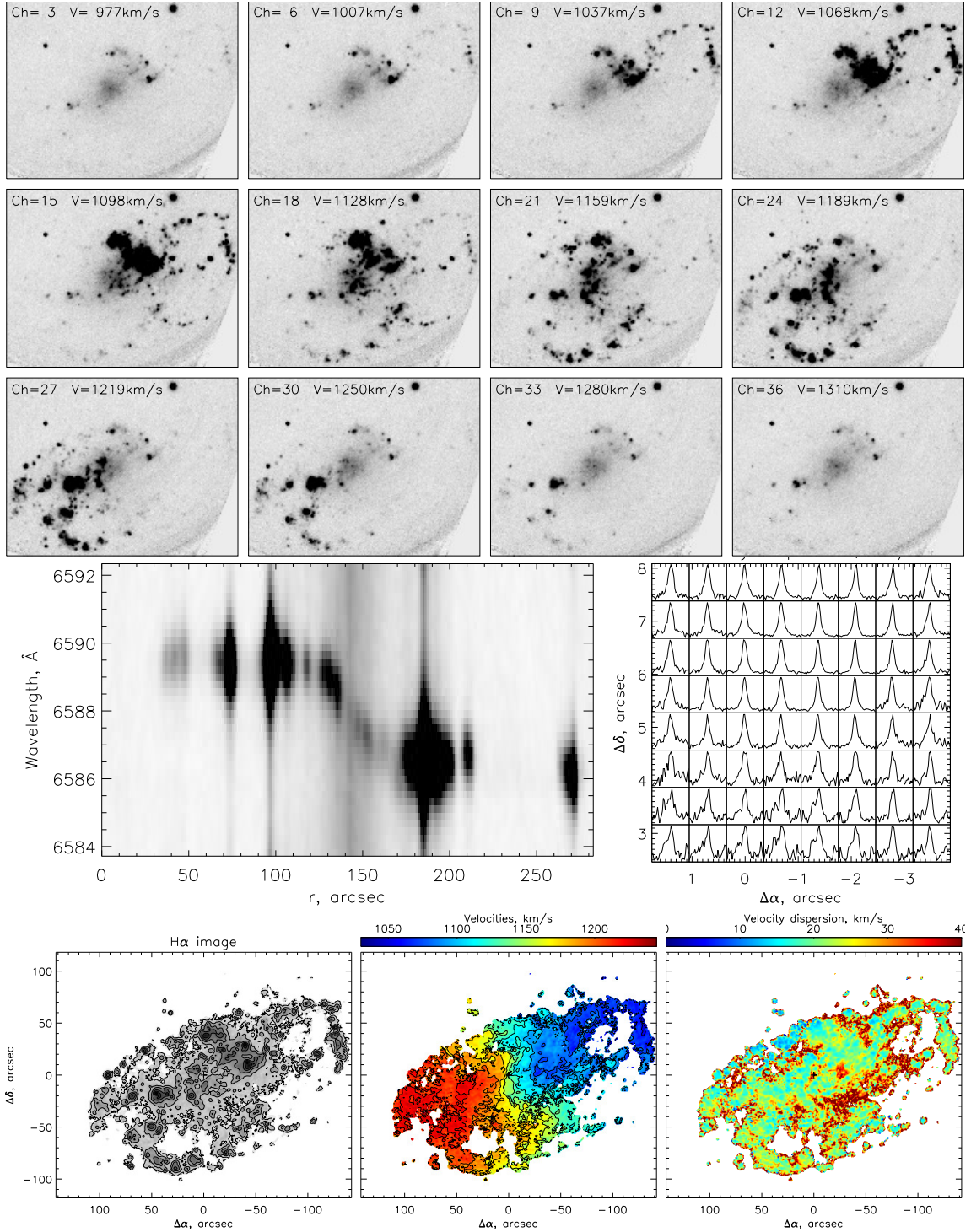


Fig. 5. Different representations of the data cube for the NGC 428 galaxy. Top: channel maps with every third channel shown. The line-of-sight velocities are labelled. Middle: the PV diagram along the major axis of the galaxy (left) and examples of H α emission-line spectra near the nucleus (right). Bottom: maps constructed as a result of approximating the spectra by the Voigt profile: emission-line flux and line-of-sight velocity, velocity-dispersion fields.

approximations (Section 4.1), and the σ line-of-sight velocity dispersion map can be used to study turbulent gas motions (Section 5). To obtain such maps, the spectral line profile is fitted by the Voigt function, which is a convolution of the Lorentz profile (describing the instrumental contour of the FPI) and the Gaussian profile (an approx-

imation of the original profile not subject to instrumental broadening). The width of the instrumental contour is determined by the calibration lines. For a more detailed description of the methodology for constructing velocity dispersion maps corrected for instrumental broadening see Moiseev & Egorov (2008).

3.3. Observations in Absorption Lines

Above we discussed only the application of the scanning FPI for 3D emission line spectroscopy of ionized gas. This is the most popular application for this technique. At the same time, FPI can obviously be used for the 3D spectroscopy in absorption lines. Overlap of the signals from neighboring orders and modulation of the observed spectrum produced by the narrow-band filter (Section 2.2 give a certain problem. It is therefore important for the spectral line studied to have a sufficiently high contrast and have no blend within the free wavelength interval of the FPI. In the 1990s, a series of successful observations of stars in globular clusters (Gebhardt et al., 1995) and selected areas toward the Milky Way bar (Rangwala et al., 2009) were made using a FPI in the Ca II $\lambda 8542$ line with the 1.5- and 4-m Cerro Tololo Inter-American Observatory telescopes. In the latter case, it was possible to measure both the line-of-sight velocities and to estimate the metallicity for more than 3000 stars from EW (Ca II). At the time, this method was a serious competitor to multi-object spectroscopy for this particular task. The same technique was used on the 0.9-m telescope of the same observatory to acquire the velocity field of the stellar component and measure the angular velocity of the bar rotation in the early-type galaxy NGC 7079 (Debattista & Williams, 2004). Note the works of the same team carried out on the CFHT telescope using the scanning FPI combined with an adaptive optics system (Gebhardt et al., 2000) to study the stellar dynamics in the center of the globular cluster M 15.

Because of the lack of filters for isolating the red calcium line, in our observations carried out with SCORPIO on the 6-m telescope we tried to measure velocities of stars in clusters by their H α absorption lines. In test observations of the globular cluster M 71 we simultaneously determined the line-of-sight velocities of about 700 stars down to $m_v \approx 18^m$, with individual measurements accurate to within $2\text{--}4\text{ km s}^{-1}$ (Moiseev, 2002). This method was subsequently applied to measure the line-of-sight velocities and identify members of open clusters of the Milky Way within the framework of A. S. Rastorguev’s application (Sternberg Astronomical Institute of Moscow State University). In 2002–2003 such measurements were carried out for several clusters, unfortunately, the results have not yet been published.

We also carried out experiments on the 6-m telescope to reconstruct the velocity fields of stars in galaxies using FPI observations in the Ca II $\lambda 6495$ line, but the accuracy of measurements proved to be low because of the low contrast of the line. On the other hand, the reflective coatings of IFP186 and IFP751 are optimized for observations, including observations in the 8500–9500 Å wavelength, and the new E2V 261-84 detector has relatively high sensitivity in this range almost without fringes. Therefore, mapping extended objects in the Ca II triplet lines with SCORPIO-2 may have interesting prospects if the appropriate filters are acquired.

4. Observational results: objects with dominating circular rotation

In this section we briefly discuss the studies made with the FPI on the 6-m telescope of galaxies whose gas kinematics is dominated by regular circular rotation. Often the aim of these studies was to search for deviations from this symmetric pattern. We therefore first discuss the methods used to extract the circular component from observational data.

4.1. Analysis of the Velocity Fields of Rotating Disks

The observed line-of-sight velocity of a point moving in an orbit tilted by angle i with respect to the sky plane is given by the following formula:

$$V_{\text{OBS}} = V_{\text{SYS}} + V_R \sin \varphi \sin i + V_\varphi \cos \varphi \sin i + V_Z \cos i, \quad (3)$$

where R and φ are the radial and azimuthal coordinates in the orbital plane, respectively; V_{SYS} is the systemic velocity, and V_φ , V_R , and V_Z are the azimuthal, radial, and vertical components, respectively, of the velocity vector.

The methods used to determine the parameters that describe the motion of ionized gas in galaxy disks from 3D spectroscopy data can be subdivided into several groups:

1. Independent search for parameters appearing in formula (3) in narrow rings of the velocity field along the radius—the “tilted ring” method.
2. Harmonic expansion of the line-of-sight velocity distribution along the azimuthal angle within narrow rings.
3. Fitting of the entire line-of-sight velocity field. It can be accompanied by the use of the map of other moments determined from the line profile (surface brightness and velocity dispersion) or results of numerical simulations.
4. Modelling of the entire data cube in the given emission line.

Let us now consider these methods in more detail.

4.1.1. Search for Parameter Values in Narrow Rings

The “tilted-ring” method was initially used to analyze the velocity field obtained from 21-cm H I radio data (Rogstad et al., 1974). Its classical description, which became the basis of the popular ROTCUR procedure included into GIPSY and AIPS radio-data reduction software, can be found in a number of papers (Begeman, 1989; Teuben, 2002). Below we briefly describe the basics of this technique adapted for the analysis of line-of-sight velocity fields of ionized gas (Moiseev et al., 2004; Moiseev, 2014b).

In the case of purely circular rotation of a thin flat disk ($V_R = V_Z = 0$, $V_\varphi = V_{\text{ROT}}$) the observed line-of-sight velocity is equal to:

$$V_{\text{OBS}}(r, PA) = V_{\text{SYS}} + V_{\text{ROT}}(R(r)) \times$$

$$\times \frac{\cos(PA - PA_{\text{kin}}) \sin i}{(1 + \sin^2(PA - PA_{\text{kin}}) \tan^2 i)^{1/2}}, \quad (4)$$

where r is the apparent distance from the rotation center in the sky plane and PA is the position angle. The distance from the rotation center in the plane of the galaxy is:

$$R(r) = r(1 + \sin^2(PA - PA_0) \tan^2 i)^{1/2} \quad (5)$$

In formula (4) PA_{kin} and PA_0 are the position angles of the kinematic axis and line-of-nodes of the disk, respectively. In the case of purely circular motions $PA_{\text{kin}} \equiv PA_0$. The observed velocity field is subdivided into elliptic rings defined by equation (5) for $R = \text{const}$. In each ring the observed dependence $V_{\text{OBS}}(PA)$ is fitted by model (4) via χ^2 minimization. As a result, we obtain for the given R the set of parameters that characterize the orientation of orbits (PA_{kin}, i), velocity of circular rotation, and systemic velocity.

If the disk is not strongly warped, we can assume that the inclination and systemic velocity do not depend on the radius ($i = i_0$, $V_{\text{SYS}} = \text{const}$), in this case radial variations PA_{kin} reflect features of the distribution of noncircular components of the velocity vector. In particular, the radial gas flows caused by the gravitational potential of the galactic bar result in a “turn” of PA_{kin} with respect to PA_0 of the disk. A comparison with the orientation of elliptical isophotes allows us to distinguish the case of a bar (i.e., a change of the shape of orbits in the galactic plane) from that of an inclined or warped disk (i.e., circular orbits in another plane)—see a discussion and references in Moiseev et al. (2004); Egorova et al. (2019).

The “tilted ring” method is quite flexible and allows one to test hypotheses about the behavior of gas motions by fixing different parameter combinations in equation (4). One can also estimate the amplitude of radial motions by setting $V_r \neq 0$ in equation (3), which is applicable for colliding ring galaxies (Bizyaev et al., 2007). Sil’chenko et al. (2019) used a modification of the method, which allows the motion of gas in strongly warped disks to be described by successive iterations even in the case of poorly filled velocity fields.

4.1.2. Harmonic Expansion

The perturbation of circular motion by non-axisymmetric gravitational potential (spiral wave, bar, tidal interaction) results in harmonic terms of the form $A_j \cos j\varphi$, $B_j \sin j\varphi$, $j = 1, 2, \dots$ appearing in the right-hand part of equation (3). In other words, the distribution of line-of-sight velocities in the narrow ring at a given radius, $V_{\text{OBS}}(\varphi)$, is expanded into a Fourier series where the systemic velocity—is the coefficient at zero harmonic, etc. Sakhibov & Smirnov (1989) were among the first to apply this idea to determine the parameters of the spiral density wave from the velocity fields acquired with FPI. Franx et al. (1994) used a similar technique to determine the shape of the gravitational potential of early-type galaxies. Lyakhovich et al. (1997) consistently described the idea of applying the method of

Fourier analysis of velocity fields to recover the full three-dimensional velocity vector of gas in the disk under certain assumptions about the nature of the spiral structure (Section 4.2). Unfortunately, the proposed method of the reconstruction of the velocity vector was not widely used. Possible reasons were the need for a very painstaking analysis involving photometric data, because the result often proved to be sensitive to the choice of the disk orientation parameters. On the other hand, the use of Fourier analysis to describe the line-of-sight velocity fields of both the gas and the stellar component in galaxies has recently become popular because of Kinemetry program (Krajnović et al., 2006). The algorithm involves generalizing the decomposition of surface brightness distributions to higher-order moments of the line-of-sight velocity distribution function: to the line-of-sight velocity (first moment), velocity dispersion (second moment), etc. Note that the method does not require the assumption of a flat disk and can be applied even to stellar-kinematics data in early-type galaxies. And in the case of gas in disk galaxies Kinemetry can be used as a high spatial frequency filter isolating the regular component of the velocity field.

4.1.3. Modelling the Entire Field

The “tilted rings” method allows one to adequately enough understand the pattern of motions in a flat disk. If the disk plane is warped, a first approximation for the warp parameters can be inferred. However, the parameter estimates obtained by fitting observations in a narrow ring by formula (4) are unstable, especially in the case of incomplete ring filling by data points with bona fide velocity measurements. First, there is a $V_{\text{ROT}}-i$ degeneracy, especially for small tilt angles $i < 30-40^\circ$. Indeed, for M rings we obtain that the total velocity field with fixed dynamical center is described by $4 \times M$ free parameters. For FPI observations of several arcmin-sized galaxies as in Fig. 5 this number can amount to several hundred (the width of the rings is close to the spatial resolution). This is obviously excessive. In practice, V_{ROT} , i , and PA_{kin} vary smoothly with radius, and simple analytical formulas for radial variations of the orbital orientation and rotation curve can be obtained by setting $V_{\text{SYS}} = \text{const}$.

Describing the velocity field in terms of a single two-dimensional model with several free parameters highly increases the stability of the solution. Thus Coccato et al. (2007) were able to describe quite well the field of gas line-of-sight velocities in the NGC 2855 and NGC 7049 galaxies based on VIMOS instrument data using a warped disk model with only seven parameters. The line of sight could cross the disk several times in the case of strong warps and therefore it was important to simultaneously take into account the brightness distribution in the emission line. We applied a similar approach to study the orientation of orbits of a highly tilted and warped disk in the Arp 212 galaxy (Moiseev, 2008). We could find a stable model so-

lution to describe the kinematics of ionized gas distributed in individual isolated H II regions.

In the case of a flat weakly perturbed disk the two-dimensional model allows its orientation parameters, even in the case of “face on” orientation ($i < 20^\circ$) to be reliably determined. An example is our FPI-based study of a nearly circular gas ring in the Hog Object (Fig. 6) with $i = 18 \pm 4^\circ$. In that case we were able to choose between a flat and a slightly warped (Finkelman et al., 2011) ring model. Another example of flat disk modelling is represented by the Fathi et al. (2006) study, which uses a stellar exponential disk model to parameterize the rotation curve.

In addition, one can directly compare the data of numerical hydrodynamic simulations with the observed velocity fields, e.g., in the case of barred galaxies (Fathi et al., 2005).

4.1.4. Modelling the Data Cube

The power of modern computers makes it possible to move from fitting two-dimensional velocity fields and brightness distributions to a more informative approximation of the entire data cube. Like in the case of the tilted-ring method, such algorithms were first applied to radio data cubes, because in the case of 21 cm line observations the spatial resolution is usually not very high and the effect of averaging the line-of-sight velocities within a synthesized beam pattern (beam smearing) is important. Given that the brightness in this line is linearly related to H I density, the intensity distribution can often be set in the form of a smooth function of radius. A good example is the popular TiRiFiC package (Józsa et al., 2007), which allows one to study warps and other features of the spatial structure of gas disks.

In the case of optical data cubes, such is primarily useful for gas kinematics in galaxies at large redshifts, where the beam smearing effect is just as important, because the spatial resolution is comparable to the size of the objects studied. Here we point out GalPak^{3D} (Bouché et al., 2015) and ^{3D}BAROLO (Di Teodoro & Fraternali, 2015) software packages. The latter can also be used to analyze the cubes obtained with the FPI (private communication). Bekiaris et al. (2016) have already demonstrated the possibility of such analysis with the GBKFIT package for the case of FPI observations of disk galaxies in the GHASP survey.

4.2. Spiral Galaxies

The first observations with FPI on the 6-m telescope (Section 2) revealed perturbations of the line-of-sight velocity fields in NGC 925 and NGC 2903 related with their spiral arms (Marcelin et al., 1982, 1983). These data were later analyzed using the method of harmonic decomposition (Sakhibov & Smirnov, 1989), which made it possible to determine the parameters of the two-arm density wave, understand the direction of radial gas motions in the arms,

and measure the pattern speed of the spirals and bar (in NGC 925). Further development of this method was stimulated by the studies of the Mrk 1040 (NGC 931) galaxy, which is distinguished by its double-peaked rotation curve with an unusually sharp jump in the rotation velocity 10 kpc from the center and noticeable non-circular motions in the disk. These peculiarities were interpreted either as an unusually large (20 kpc) bar, invisible due to dust extinction in the strongly inclined disk (Amram et al., 1992), or as the presence of vortex structures (Afanasiev & Fridman, 1993). The latter interpretation is associated with the hypothesis of hydrodynamic generation of spiral waves in the gaseous disk (Morozov, 1979), an alternative to the classical stellar disk density wave theory. The hydrodynamic mechanism required an abrupt jump of rotation velocity similar to that observed in Mrk 1040, which is also reproduced in laboratory experiments on rotating shallow water (Fridman et al., 1985). Giant vortices rotating in the direction opposite that the rotation of the galaxy (anticyclones) should also be observed in the coordinate system associated with spirals in the case of the classical generation mechanism. However, their location differs from what is predicted by hydrodynamic theory. The corresponding criteria can be found in the paper by Lyakhovich et al. (1997) dedicated to the method of reconstructing the pattern of three-dimensional gas motions on the basis via Fourier analysis of velocity fields.

Within the framework of the joint ‘Vortex’ project (SAO RAS, INASAN RAS, and SAI MSU) several dozen velocity fields were acquired using observations made on the 6-m telescope and Fourier analysis was performed for them. Unfortunately, only the results of the reconstruction of three-dimensional velocity vectors in the disks of spiral galaxies NGC 157 (Fridman et al., 2001a) and NGC 3631 (Fridman et al., 1998, 2001b) have been published. In both cases, giant vortex structures associated with the classical density wave generation mechanism were found. Also Fridman et al. (2005) published the results of the analysis of the kinematics of the other 15 galaxies of the sample using “tilted ring” method. For these objects the rotation curves were constructed free from the influence of non-circular motions, and numerous regions with peculiar kinematics of ionized gas were identified where the deviations from circular rotation amount to $50\text{--}150\text{ km s}^{-1}$. Two kinematic components in the line-of-sight projection are observed in some cases. Such large peculiar velocities are not associated with spiral waves, but are rather due to either “galactic fountains” caused by star formation (section 5), or interactions with the environment, including accretion of gas clouds. Some of these peculiar regions were detected during the early long-slit spectrograph observations on the 6-m telescope (Afanasiev et al., 1988, 1992), while FPI allowed them to be studied in detail.

Of interest is the NGC 1084 galaxy with a complex structure of emission-line profiles found in its periphery. In this galaxy the brightest in the H α system of H II-regions looks like an emission “spur” extending perpendicular to

the spiral arm⁵. A peculiar component in $H\alpha$, shifted relative to the main component by $-100...+150 \text{ km s}^{-1}$ and often accompanied by shock excitation in the $[N II]$ line is observed between the $H II$ regions. Moiseev (2000) suggested two interpretations of the observed picture associated both with galactic fountains and traces of past interactions. Further evidence for both recent ($< 40 \text{ Myr}$, Ramya et al., 2007) and the earlier ($\sim 1 \text{ Gyr}$ Martínez-Delgado et al., 2010) merger of a dwarf satellite emerged later.

Non-circular gas motions can be caused not only by spiral density waves, but also by the triaxial gravitational potential of the bar. The perturbation of the velocity field turns PA_{kin} with respect to the PA of outer isophotes, and this effect is reproduced in numerical simulations (see Moiseev & Mustsevoi, 2000; Moiseev et al., 2004, and references there), allowing circumnuclear bars (minibars) to be detected inside the central kiloparsec, even in the cases where the bar is not visible in optical images. One of the first studies aimed at searching for circumnuclear bars via 3D spectroscopy (Zasov & Sil’chenko, 1996) used, among other data, observations made with the FPI attached to the 6-m telescope. The case of the NGC 972 galaxy is quite illustrative, where the bar in the dust-obscured central region was first detected by the velocity-field perturbation it caused, and then found in near-IR images free from dust extinction (Zasov & Moiseev, 1999). A systematic difference between $H\alpha$ and $[N II]$ emission-line line-of-sight velocities due to the shock at the bar edges was found in the same galaxy (Afanasiev et al., 2001). The effect of lower rotation velocities in the forbidden lines at the bar edges was described earlier in Afanasev & Shapovalova (1981); Afanasev & Shapovalova (1994). Unfortunately, this line of research has not been further developed. Author believes that a comparison of line-of-sight velocities in the Balmer and forbidden lines can be used to study the properties of galactic bars in modern 3D spectroscopic surveys.

We should also point out the work of Smirnova et al. (2006) who used SCORPIO FPI data to measure the bar pattern speed in the NGC 6104 galaxy and study candidate galaxies with double bars based on the combined FPI and MPFS data set (Moiseev et al., 2004).

An analysis of the line-of-sight velocity field can be used to construct sufficiently reliable rotation curves with a confident determination of the tilt angle i , free from the influence of regions of noncircular motions. This is important for building models of mass distribution in galaxies. One of the first works of this kind carried out on the 6-m telescope to be noted is the paper by Ryder et al. (1998), which is also one of the first examples of the simultaneous use of the data for ionized gas ($H\alpha$ -line FPI data) and neutral hydrogen (21-cm line observations) to study velocity fields. These data complement each other well because the disk is more extended in $H I$, but the spatial resolution of such observations is insufficient to explore the interior regions where $H\alpha$ -line measurements are helpful. Moiseev

(2014b) performed such a match of rotation curves for a number of nearby dwarf galaxies.

4.3. Early-Type Galaxies (E-S0)

In recent decades, the old point of view that elliptical and lenticular galaxies contain no cold and warm gas has been changing. Optical 3D spectroscopy including observations performed on the 6-m telescope has played an important role in this process. Plana & Boulesteix (1996); Plana et al. (1998) studied the distribution and kinematics of ionized gas in 11 E- and S0-type galaxies. In three cases, two kinematically distinct gaseous subsystems were found, possibly located in different basic planes of the ellipsoids, in what is a clear indication of an external origin of the gas. Subsequent integral-field spectroscopy of lenticular galaxies brought significantly advances to the study of the stellar population and ionized gas of early-type galaxies, but the relatively small field of view prevented the study of their outer parts. There were no such limitations in the study by Sil’chenko et al. (2019), who presented the results of SCORPIO/SCORPIO-2 observations of extended gaseous disks in 18 lenticular galaxies made using 3D (FPI) and long-slit spectroscopy (see the case of NGC 3414 shown in Fig. 6). Ongoing star formation appears to usually occur where gas lies exactly in the mid-plane of the stellar disk and follows a circular rotation. In galaxies with no ongoing star formation extended gaseous disks are either in a dynamically stable quasi-polar orientation or are a result of the capture of matter having a different direction of angular momentum, which leads to shock ionization gas. The available data are indicative of a significant difference between the geometry of gas accretion in lenticular and spiral galaxies: accretion in S0-type galaxies is typically off-plane.

4.4. Polar-Ring Galaxies and Related Objects

Another example of external gas structures are polar ring galaxies (PRGs). Here extended rings or disks of gas, dust, and stars rotate in a plane approximately perpendicular to the main galactic disk. The formation of the PRGs is believed to be due to capture of matter with a different orbital momentum: a merger of two galaxies, accretion of the satellite matter or gaseous filaments by the host galaxy. Photometric and spectroscopic study of PRGs with the 6-m telescope was initiated by a team of researchers from St. Petersburg University back in the 1990s. Later, the researchers started using 3D spectroscopic techniques to study the most morphologically complex PRG candidates from the catalog of Whitmore et al. (1990). Note that both methods available on the 6-m telescope were combined. MPFS was used to study the kinematics of the stellar population of the central galaxy inside a $16'' \times 16''$ field. The velocity field of ionized gas was mapped using a wide-field FPI. Where necessary, the analysis was supplemented with photometric and long-slit

⁵ NED now refers to this region as “NGC 1084 spur”.

spectroscopy (Hagen-Thorn et al., 2005; Merkulova et al., 2009, 2012). A characteristic example is represented by UGC 5600, where most of the gas lies outside the plane of the stellar disk and in the case of inner regions were are dealing with a polar ring, whereas in the outer regions we have a strongly warped gaseous disk (Shalyapina et al., 2007). Shalyapina et al. (2004a) used similar observations of the NGC 7468 galaxy to detect a circumnuclear polar disk of radius of about 1 kpc. The catalog and characteristic parameters of such structures associated with PRGs are presented in Moiseev (2012). In some cases, the analysis of the velocity fields of gas and stars led to the exclusion of the galaxy from the list of PRG candidates (Yakovleva et al., 2016).

In the case of a flattened or triaxial gravitational potential, stable orbits exist in the polar plane, and hence the captured matter should rotate there long enough. If the orbital plane is significantly different from the polar plane, the nascent ring must precess toward the galactic plane. Thus FPI observations of the Arp 212 galaxy in H α IFP showed the two rotating subsystems of ionized gas to coexist there: the inner disk, which coincides with the stellar disk, and the outer H II regions with highly inclined orbits (Moiseev, 2008). Given the published data on the H I distribution, we conclude that most of the gas in the galaxy is concentrated in a wide ring with a radius of about 20 kpc. The outer parts of the ring rotate in a plane orthogonal to the stellar disk. The orbits of the gas clouds precess with decreasing radius and approach the disk plane. In the 2–3.5 kpc interval of galactocentric distances a collision of the polar ring gas and the inner disk is observed, which is accompanied by a burst of star formation.

The problem of non-coplanar gaseous subsystems, including the colliding ones, in late-type galaxies was considered in Moiseev (2011, 2014a). An analysis of the FPI maps for 25 nearby dwarf galaxies presented in Moiseev (2014b) showed that the fraction of objects with inclined gas structures is greater than 10%, i.e. exceeds the available estimates of the occurrence rate of “classical” PRGs by more than one order. This fact is indicative of the important role played by accretion of external matter in the current evolution of galaxies.

New digital sky surveys have increased the list of bona fide PRG candidates available for detailed study (e.g., SPRC catalog Moiseev et al., 2011). Observations of the rotation of gas and stars in two mutually perpendicular planes make it possible to study the three-dimensional distribution of mass in the galaxy, and, in particular, determine the shape of the dark halo: its flattening, and deviations from axial symmetry. Khoperskov et al. (2014) were able to reconstruct the shape of the dark halo of the SPRC-7 galaxy from the observations of Brosch et al. (2010) with SCORPIO, including those made in the FPI mode. This galaxy has one of the largest polar rings, about 50 kpc in diameter. Its dark halo appears to be markedly flattened toward the ring plane (Fig. 7). (Khoperskov et al., 2013) performed a similar analysis for

SPRC-260 based FPI observations. More details about the results of observations SPRC objects using different techniques can be found in (Moiseev et al., 2015a). In recent years, FPI on the 6-m telescope was used to map ionized gas in several more galaxies of this catalog and the data are being prepared for publication.

A spectroscopic study of the known ring galaxy, Hoagg’s Object, performed on the 6-m telescope (Fig. 6) showed that although the central galaxy and the outer ring rotate in the same plane, but the formation mechanism of the system formation is close to that proposed for some PRGs. The observed properties of Hoag’s Object can be explained assuming that the ring formed via “cold” accretion of gas from intergalactic medium filaments onto the progenitor, an elliptical galaxy (Finkelman et al., 2011). Subsequent 21-cm observations (Brosch et al., 2013) are also consistent with this hypothesis.

4.5. Interacting and Peculiar Systems

The study of the velocity fields of colliding ring galaxies, including the results of numerical simulations, makes it possible to determine the expansion velocity of the ring density wave. An interesting example is Arp 10 with two star-forming rings (Bizyaev et al., 2007). An analysis of the velocity field in this galaxy revealed significant (more than 30 km s^{−1}) vertical oscillations of the gaseous disk in the inner ring. At the same time, the outer ring expands irregularly, with a velocity of $V_r = 30\text{--}110\text{ km s}^{-1}$, which explains its elliptical shape of the ring. It is shown that the ring structure formed as a result of a non-central collision with a massive companion 85 Myr ago. Examples of velocity fields of other colliding ring galaxies obtained via FPI observations on the 6-m telescope can be found in Moiseev & Bizyaev (2009).

An interesting and so far poorly studied aspect of galaxy interactions has been found in observations of Mrk 334 carried out on the 6-m telescope (Smirnova & Moiseev, 2010). This galaxy recently underwent a merger with a massive companion. A cavern filled with low-density ionized gas with significant deviations from circular motion (up to 70 km s^{−1} according to the FPI maps) was found in the galaxy disk. We interpreted this region as the sites of a recent (about 12 Myr ago) passage of the remains of a disrupted satellite through the gaseous disk of the host galaxy. Also remarkable are the results of a joint analysis of photometric and spectroscopic data for the Mrk 315 galaxy (Ciroi et al., 2005), which is caught at the time of its interaction with two companions, resulting in the appearance of several kinematic components in the FPI data cube. At the same time, one of the companions, in the process of a fast passage through the gaseous halo of the galaxy, loses its own gas, forming a structure similar to the contrail of an aircraft.

The studies carried out using the 6-m telescope focused significantly investigating the kinematics of dwarf galaxies and their interactions with environment. Moiseev

et al. (2010) performed FPI observations of a sample of nine galaxies with extremely low gas metallicity (1/35 to 1/10 of the solar $[\text{O}/\text{H}]$ value). The velocity fields in most galaxies cannot be described by a model of a single rotating disk, the observed noncircular velocities are indicative of different stages of interaction or merger with the companion, in two cases we were able to identify two independently rotating subsystems. All this suggests that the current burst of star formation in these galaxies is induced by a recent interaction. A typical example is DDO 68, which has a record low metallicity among nearby galaxies and exhibits signs of unfinished interaction (see Pustilnik et al., 2017, and references therein).

A program of FPI mapping of a sample of metal-poor dwarf galaxies in nearby voids is currently carried out on the 6-m telescope. (Egorova et al., 2019) described the principles of selecting objects and analyzed the kinematics of the brightest galaxy of the sample—NGC 428 (Fig. 5). In this galaxy, like in the in the example discussed above traces of ongoing interactions with companions or accretion of external gas are observed despite the relatively scarce environment. Thus the complex structure of the Ark 18 galaxy proved to be a result of two successive mergers with companions, one of which, having a 1/5 mass ratio, produced the outer low surface brightness disk (Egorova et al., 2021).

4.6. Active Galactic Nuclei

Analysis of ionized gas in galaxies with active nuclei has since long been the focus of interest of our team at SAO RAS. The first observations were carried out with a long-slit spectrograph (see for example Afanasiev & Shapovalova, 1981; Afanasiev & Sil’chenko, 1991). However, the developed 3D spectroscopy instruments demonstrated the high efficiency of these techniques for studying emission features with complex morphology, perturbed kinematics, and ambiguous ionization states. The Seyfert galaxy Mrk 573 was studied using both types of 3D spectrographs available on the 6-m telescope (Afanasiev et al., 1996): MPFS for the spectroscopy of the central region in a wide wavelength interval and a scanning FPI for mapping the kinematics of ionized gas without restrictions on the field of view. This approach was further applied in a series of works aimed at the study of both the processes of feeding gas to the central regions of galaxies (Smirnova et al., 2006) and the impact of the active nucleus on the interstellar medium due to Mrk 533 radio jets (Smirnova et al., 2007), galactic wind outflows (see also Smirnova & Moiseev, 2010; Afanasiev et al., 2020) or ionization cones (Smirnova et al., 2018; Kozlova et al., 2020). In many cases we are dealing with so-called extended emission-line regions (EELRs) with sizes ranging from several to tens of kiloparsecs.

A team from SAO RAS in cooperation with researchers from Volgograd State University developed an original scenario explaining the formation of cones of ionized

matter in the neighborhood of nuclei of Seyfert galaxies including Z-shaped features observed in a number of EELRs. We assumed in that study that regular ionized features are associated with shocks generated by the Kelvin-Helmholtz instability during the intrusion of the jet emerging from the active nucleus into the surrounding environment (Afanasiev et al., 2007a). Afanasiev et al. (2007b) performed the corresponding numerical computations reproducing the EELR morphology in NGC 5252. However, in most cases observations indicate that the cones is mainly ionized by the hard ultraviolet emission of the nucleus collimated by the dust torus. Note that the beam of such an “ionization lighthouse” can illuminate gas far away from the galaxy. Thus in Mrk 6 emission filaments are observed out to 40 kpc from the nucleus, and their velocity field shows that here we are dealing with accretion of external matter rather than with nuclear outflow (Smirnova et al., 2018).

In the case of a lucky orientation with respect to the observer EELRs serve as a kind of remote screen reflecting the past ionization activity of the nucleus, as in the case of the prototype “fading” active galactic nuclei—Hanny’s Voorwerp (IC 2497 Lintott et al., 2009). Combined observations of a sample of candidate fading active galactic nuclei proved this explanation for the existence and the nature of EELRs located beyond 10 kpc from the center of the galaxy. (Keel et al., 2015). The kinematic maps based on the results of FPI observations demonstrated that the ionized gas has low velocity dispersion and generally follows a circular rotation pattern. Hence we are dealing with ionization of intergalactic gas, which is often associated with tidal structures, rather than outflow. Figure 6 shows the UGC 7342 galaxy, where gas at large galactocentric distances rotates regularly, and perturbations associated with the nuclear outflow are observed only within the central kiloparsec (Keel et al., 2017).

5. Observational results: effects of star formation on the ambient gas

5.1. Galactic Wind

The most global feedback of ongoing star formation has on the interstellar medium is the galactic wind (superwind)—conical gas outbursts from the galactic plane driven by collective supernova explosions in the circumnuclear region. Wind structures can be best seen in the high inclined galactic disk, but in that case the observed line-of-sight velocities are dominated by circular rotation, as in the velocity field of NGC 4460 shown in Fig. 6. The geometric wind model in this galaxy considered by Oparin & Moiseev (2015) yields an outflow velocity range of $30\text{--}80\text{ km s}^{-1}$, which is less than the escape velocity from the galaxy. Therefore after cooling down the swept-out matter falls back onto the disk. The same approach to the analysis of FPI data combined with IFS PPAK data from CALIFA survey was applied to study the wind in UGC10043 (López-Cobá et al., 2017). Our estimate of

the outflow velocity ($100\text{--}250\text{ km s}^{-1}$) is consistent with that inferred in terms photoionization models from the emission-lines ratios in the BPT diagrams (Baldwin et al., 1981). An important feature of the galactic wind is the high turbulence of gas, which shows up as the increase of velocity dispersion along the line of sight (σ). The spectroscopic resolution of our FPIs is high enough to trace the increase of σ with the distance from the disk plane. This can also be seen in the archival observations of the NGC 6286 galaxy, where Shalyapina et al. (2004b) found superwind for the first time and this finding was recently confirmed in CALIFA (López-Cobá et al., 2019).

Shocks in the case of galactic winds and less powerful “galactic fountains” result in an increase of both σ and the observed luminosity in forbidden lines. Therefore, the simultaneous use of kinematic data based on high-resolution FPI observations combined with emission-line flux data obtained from long-slit or integral-field spectroscopy can be used to diagnose the interstellar medium in galaxies, by unambiguously distinguishing regions of shock ionization. This technique, which we call “BPT- σ ”, has been successfully tested in the analysis of galaxy data cubes observed with MPFS and PPAK instruments (López-Cobá et al., 2017; Oparin & Moiseev, 2018).

5.2. Gas in Star-Forming Regions

Moiseev et al. (2015b) used the scanning FPI mounted on the 6-m telescope to map the distribution of the line-of-sight velocity dispersion of ionized gas in a large sample of nearby dwarf galaxies (see the example of UGCA 92 shown in Fig. 8. We demonstrated the existence of a global relation between the current star-formation rate (SFR) and the brightness-averaged velocity dispersion. This relation is fulfilled over a very wide range of SFR values (5.5 orders of magnitude) and is obeyed both by rotation-supported disks and individual giant H II regions. We interpreted this fact as indicating that σ in dwarf galaxies does not reflect virial motions, but is mostly determined by the energy injected into the interstellar medium in the process of star formation. The acquired data about turbulent gas motions in nearby galaxies are now used to construct unified models of galaxy disks (Krumholz et al., 2018).

Yang et al. (1996) and Munoz-Tunon et al. (1996) suggested using FPI maps to construct the “intensity—velocity dispersion” ($I - \sigma$) diagrams. These diagrams make it possible not only to study expanding envelopes associated with star-forming regions (Martínez-Delgado et al., 2007), but also identify unique objects: supernova remnants, emission-line stars, etc. For a detailed description of this technique see the paper by Moiseev & Lozinskaya (2012), who found a candidate LBV star in UGC 8508.

In the case of dIrr galaxies of the Local Universe, the angular scale is $3\text{--}20\text{ pc}''$, and hence FPI observations allow detailed study of the dynamics of the processes leading to the increase of gas velocity dispersion: supernova

remnants and shells associated with winds emerging from star-forming regions. The absence of spiral density waves and the large thickness of their gaseous disks make dIrr galaxies optimal laboratories for studying the stellar feedback. Such works were started on the 6-m telescope at the initiative of T. A. Lozinskaya (Sternberg Astronomical Institute of Moscow State University) with the study of the IC 1613 galaxy, where shells of ionized gas are associated with large-scale HI structures (Lozinskaya et al., 2003). Here, we were among the first to analyze FPI data (Section 3.2) jointly with 21-cm HI line data cubes using the technique of PV diagrams. This approach made it possible to determine the dynamic ages of the shells and compare them with the ages of the central star clusters. This line of research was further developed to the study of giant (up to 1 kpc in diameter) HI supershells in a number of dwarf galaxies, where the energy of the central star clusters was evidently insufficient to produce such structures. This phenomenon is now explained by triggered star formation in dense walls of supershells. Observations with FPI allow this process to be studied in detail. For a detailed review, see Egorov et al. (2015) and recent papers on Holmberg I and II (Egorov et al., 2017b, 2018) galaxies.

5.3. Emission-Line Stars and Unique Objects

Concerning the study of nebulae surrounding individual stars, we first point out the measurements of the dynamic ages of the giant bipolar envelope (its size is greater than 200 pc) surrounding the unique WO star (Afasiev et al., 2000) in IC 1613 and a possible hypernova remnant — a synchrotron supershell in the IC 10 galaxy (Lozinskaya & Moiseev, 2007). At the center of the candidate hypernova remnant there is an X-ray source—IC10 X-1—a binary consisting of a WR star and a massive ($23\text{--}24\text{ M}_{\odot}$) black hole. In recent years, interest in such objects has increased due to the detection of gravitational waves from merging black holes (see discussion in Bogomazov et al., 2018).

Interesting results were obtained in FPI studies of the nebulae associated with ultrabright X-ray sources (ULXs) in the Holmberg IX (Abolmasov & Moiseev, 2008) and Holmberg II (Egorov et al., 2017a) galaxies. In the latter case, an analysis of the velocity fields in the lines [O III], [S II] and H α revealed a structure interpreted as a manifestation of a bow shock caused by a fast ULX moving through the interstellar medium and the influence of its hot wind on the nebula. Observations can be best explained assuming that the ULX escaped the central part of the nearby cluster at a velocity of about 70 km s^{-1} . This supports the hypothesis that many ULXs are accreting stellar-mass black holes (Poutanen et al., 2013). Note also the mapping of supersonic gas flows in the nebula related with the SS433 object (Abolmasov et al., 2010).

Similar to the case of Holmberg II ULX, data on the line-of-sight velocities and brightness distribution in the

CTB 80 pulsar nebula (Fig. 8) were used to estimate the space velocity of the pulsar (Lozinskaya et al., 2005).

Long-term observations of Herbig–Haro outflows associated with young stellar objects make it possible to measure the proper motions of individual details in the FPI data cube. Observations with a scanning FPI revealed the complex kinematics in the outflow from HL Tau (Movsessian et al., 2007): compact clumps with high line-of-sight velocity (-150 km s^{-1}) and bow-shock structures in front them with comparatively low velocity (-50 km s^{-1}). Two epochs of FPI observations (2001 and 2007) were used to measure the proper motions of spectrally selected structures with different line-of-sight velocities. The tangential velocities of both features are the same and equal to about 160 km s^{-1} . This result suggests that the features in the outflow from HL Tau is a result of episodic mass ejections, accompanied by the observed emission of the clump of high-speed gas and an arc-shaped shock in front of it (Movsessian et al., 2012). Fig. 8 shows an example of a similar study of FS Tau (Movsessian et al., 2019).

FPI observations of Galactic nebulae associated with massive stars performed on the 6-m telescope are rather episodic, e.g., observations of the Herbig star S 235B (Boley et al., 2009) and the nebula surrounding the MWC 137 supergiant (Fig. 8). In the latter case, bow-shock structures were found outside the field previously investigated with MUSE at VLT (Kraus et al., 2021). Similar observations continue, we expect interesting results.

6. Conclusion

Boulesteix (2002) compared 3D spectroscopy instruments in the “field of view—spectral resolution” plane. Figure 9 presents such a diagram, which shows \mathcal{R} and FOV for all scanning FPI from Table 1. A number of integral-field spectrographs of 3.6–10-m telescopes are shown for comparison: MUSE (Bacon et al., 2014) and blueMUSE (Jeanneau et al., 2020), PPAK (Kelz et al., 2006), GMOS (Allington-Smith et al., 2002), and the two configurations of KCWI (Morrissey et al., 2018).

It is evident from the above diagram that even now, in the era of sweeping development of 3D spectroscopy techniques, scanning FPI-based systems remain unrivaled⁶ for the combination of a large field of view ($FOV > 100''$) and high angular resolution ($\mathcal{R} > 10\,000$). This defines at least one important area of research, including studies performed on the 6-m telescope of SAO RAS—the study of ionized gas motions in large fields (Milky Way nebulae and nearby galaxies). A certain problem is the subtraction of the sky background in cases where the entire field of view is occupied by an emission object, but new algorithms of

data analysis should help in this case. In particular, there is a positive experience with the construction of FPI mosaics, for example, in the study of emission envelopes in the stellar association Cyg OB1 (Sitnik et al., 2019).

Our experience in the study of various Galactic and extragalactic objects with a scanning FPI shows that this technique is most efficient when combined with other methods of 3D spectroscopy and with radio interferometry data. Observations on the 6-m telescope with a scanning FPI as a part of SCORPIO-2 show that these data can complement the fundamentally new and important information acquired with IFS like MUSE, PPAK and MaNGA. Our team at SAO RAS is open to discuss any new collaborative research projects involving scanning FPIs.

Acknowledgements. The author is grateful to his colleagues from the Laboratory of spectroscopy and photometry of extragalactic objects of SAO RAS, colleagues, professors and students who coauthored the papers mentioned in this review for their assistance. Special thanks are due to S. N. Dodonov and A. A. Smirnova for their comments that allowed the author to improve the manuscript. The paper is dedicated to the memory of V. L. Afanasiev whose enthusiasm and work made it possible to create SCORPIO and SCORPIO-2 instruments.

Fundings

The work was carried out within the framework of the government contract of SAO RAS approved by the Ministry of Science and Higher Education of the Russian Federation. Observations on the 6-m telescope of SAO RAS are supported by the the Ministry of Science and Higher Education of the Russian Federation (including contract No. 05.619.21.0016, unique project identifier RFMEFI61919X0016).

References

- Abolmasov, P., Maryeva, O., & Burenkov, A. N. 2010, *Astronomische Nachrichten*, 331, 412
- Abolmasov, P. & Moiseev, A. V. 2008, *Rev. Mex. Astron. Astrofis.*, 44, 301
- Afanasiev, V. L. & Shapovalova, A. I. 1981, *Astrofizika*, 17, 403
- Afanasiev, V. L., Balega, Y. Y., Grudzinsky, M. A., et al. 1987, in ser. *Tekhnika teledidenia*, Vol. 5, “Tekhnika sredstv svyazi”, ed. (in Russian), 13
- Afanasiev, V. L., Boulesteix, J., Bonnarel, F., Dodonov, S., & Vlasjuk, V. 1990a, in *Dynamics and Interactions of Galaxies*, ed. R. Wielen, 354–355
- Afanasiev, V. L., Burenkov, A. N., Shapovalova, A. I., & Vlasjuk, V. V. 1996, in *Astronomical Society of the Pacific Conference Series*, Vol. 91, IAU Colloq. 157: *Barred Galaxies*, ed. R. Buta, D. A. Crocker, & B. G. Elmegreen, 218
- Afanasiev, V. L., Burenkov, A. N., Zasov, A. V., & Sil’chenko, O. K. 1988, *Astrofizika*, 28, 243

⁶ An example of an instrument combining an extended spectral range, high resolution and large field of view is the SITELE Fourier spectrograph on CFHT (Drissen et al., 2019). However, this technique also has its limitations and is not yet very common on telescopes.

- Afanasiev, V. L., Burenkov, A. N., Zasov, A. V., & Silchenko, O. K. 1992, *AZh*, 69, 19
- Afanasiev, V. L., Dodonov, S. N., Khrapov, S. S., Mustsevoi, V. V., & Moiseev, A. V. 2007a, *Astrophysical Bulletin*, 62, 1
- Afanasiev, V. L., Dodonov, S. N., Khrapov, S. S., Mustsevoi, V. V., & Moiseev, A. V. 2007b, *Astrophysical Bulletin*, 62, 15
- Afanasiev, V. L., Dodonov, S. N., & Moiseev, A. V. 2001, in *Stellar Dynamics: from Classic to Modern*, ed. L. P. Ossipkov & I. I. Nikiforov, 103
- Afanasiev, V. L. & Fridman, A. M. 1993, *Astronomy Letters*, 19, 319
- Afanasiev, V. L., Lozinskaya, T. A., Moiseev, A. V., & Blanton, E. 2000, *Astronomy Letters*, 26, 153
- Afanasiev, V. L. & Moiseev, A. V. 2005, *Astronomy Letters*, 31, 194
- Afanasiev, V. L. & Moiseev, A. V. 2011, *Baltic Astronomy*, 20, 363
- Afanasiev, V. L., Moiseev, A. V., & Smirnova, A. A. 2020, *Astrophysical Bulletin*, 75, 12
- Afanasiev, V. L. & Shapovalova, A. I. 1994, in *Mass-Transfer Induced Activity in Galaxies*, ed. I. Shlosman, 95
- Afanasiev, V. L. & Sil'chenko, O. K. 1991, *Astrofizicheskie Issledovaniia Izvestiya Spetsial'noj Astrofizicheskoy Observatorii*, 33, 88
- Afanasiev, V. L., Vlasjuk, V. V., Dodonov, S. N., & Sil'chenko, O. K. 1990b, Preprint of the SAO RAS, 54, 1
- Allington-Smith, J., Murray, G., Content, R., et al. 2002, *PASP*, 114, 892
- Amram, P., Marcelin, M., Bonnarel, F., et al. 1992, *A&A*, 263, 69
- Ardiljanov, V. I., Murzin, V. A., Afanasieva, I. V., Ivaschenko, N. G., & Pritychenko, M. A. 2020, in *Ground-Based Astronomy in Russia. 21st Century*, ed. I. I. Romanyuk, I. A. Yakunin, A. F. Valeev, & D. O. Kudryavtsev, 115–118
- Arribas, S., Mediavilla, E., & Rasilla, J. L. 1991, *ApJ*, 369, 260
- Atherton, P. D. 1995, in *Astronomical Society of the Pacific Conference Series*, Vol. 71, IAU Colloq. 149: Tridimensional Optical Spectroscopic Methods in Astrophysics, ed. G. Comte & M. Marcelin, 50
- Bacon, R., Adam, G., Baranne, A., et al. 1995, *A&AS*, 113, 347
- Bacon, R., Vernet, J., Borisova, E., et al. 2014, *The Messenger*, 157, 13
- Baldwin, J. A., Phillips, M. M., & Terlevich, R. 1981, *PASP*, 93, 5
- Begeman, K. G. 1989, *A&A*, 223, 47
- Bekiaris, G., Glazebrook, K., Fluke, C. J., & Abraham, R. 2016, *MNRAS*, 455, 754
- Bizyaev, D. V., Moiseev, A. V., & Vorobyov, E. I. 2007, *ApJ*, 662, 304
- Bland, J. & Tully, R. B. 1989, *AJ*, 98, 723
- Bogomazov, A. I., Cherepashchuk, A. M., Lipunov, V. M., & Tutukov, A. V. 2018, *New Astronomy*, 58, 33
- Boley, P. A., Sobolev, A. M., Krushinsky, V. V., et al. 2009, *MNRAS*, 399, 778
- Bouché, N., Carfantan, H., Schroetter, I., Michel-Dansac, L., & Contini, T. 2015, *AJ*, 150, 92
- Boulesteix, J. 2002, in *Astronomical Society of the Pacific Conference Series*, Vol. 282, *Galaxies: the Third Dimension*, ed. M. Rosada, L. Binette, & L. Arias, 374
- Boulesteix, J., Georgelin, Y., Marcelin, M., & Fort, J. A. 1982, in *Astrophysics and Space Science Library*, Vol. 92, IAU Colloq. 67: Instrumentation for Astronomy with Large Optical Telescopes, ed. C. M. Humphries, 223–227
- Boulesteix, J., Georgelin, Y., Marcelin, M., & Monnet, G. 1984, in *Society of Photo-Optical Instrumentation Engineers (SPIE) Conference Series*, Vol. 445, *Instrumentation in astronomy V*, ed. A. Boksenberg & D. L. Crawford, 37–41
- Boulesteix, J., Georgelin, Y. P., Lecoarer, E., Marcelin, M., & Monnet, G. 1987, *A&A*, 178, 91
- Brosch, N., Finkelman, I., Oosterloo, T., Jozsa, G., & Moiseev, A. 2013, *MNRAS*, 435, 475
- Brosch, N., Kniazev, A. Y., Moiseev, A., & Pustilnik, S. A. 2010, *MNRAS*, 401, 2067
- Buisson, H., Fabry, C., & Bourget, H. 1914, *ApJ*, 40
- Ciampa, D. A., Barger, K. A., Lehner, N., et al. 2021, *ApJ*, 908, 62
- Ciroi, S., Afanasiev, V. L., Moiseev, A. V., et al. 2005, *MNRAS*, 360, 253
- Coccato, L., Corsini, E. M., Pizzella, A., & Bertola, F. 2007, *A&A*, 465, 777
- Courtès, G. 1960, *Annales d'Astrophysique*, 23, 115
- Courtes, G. 1982, in *Astrophysics and Space Science Library*, Vol. 92, IAU Colloq. 67: Instrumentation for Astronomy with Large Optical Telescopes, ed. C. M. Humphries, 123
- Daigle, O., Carignan, C., Hernandez, O., Chemin, L., & Amram, P. 2006, *MNRAS*, 368, 1016
- de Vaucouleurs, G. & Pence, W. D. 1980, *ApJ*, 242, 18
- Debattista, V. P. & Williams, T. B. 2004, *ApJ*, 605, 714
- Di Teodoro, E. M. & Fraternali, F. 2015, *MNRAS*, 451, 3021
- Dodonov, S. N., Vlasjuk, V. V., & Drabek, S. V. 1995, *Fabry-Perot interferometer. User Manual*
- Drissen, L., Martin, T., Rousseau-Nepton, L., et al. 2019, *MNRAS*, 485, 3930
- Egorov, O. V., Lozinskaya, T. A., & Moiseev, A. V. 2015, *Astronomical and Astrophysical Transactions*, 29, 17
- Egorov, O. V., Lozinskaya, T. A., & Moiseev, A. V. 2017a, *MNRAS*, 467, L1
- Egorov, O. V., Lozinskaya, T. A., Moiseev, A. V., & Shchekinov, Y. A. 2017b, *MNRAS*, 464, 1833
- Egorov, O. V., Lozinskaya, T. A., Moiseev, A. V., & Smirnov-Pinchukov, G. V. 2018, *MNRAS*, 478, 3386
- Egorova, E. S., Egorov, O. V., Moiseev, A. V., et al. 2021, *MNRAS*, 504, 6179
- Egorova, E. S., Moiseev, A. V., & Egorov, O. V. 2019, *MNRAS*, 482, 3403

- Epinat, B., Amram, P., & Marcelin, M. 2008, *MNRAS*, 390, 466
- Fabry, C. & Perot, A. 1901, *ApJ*, 13, 265
- Fathi, K., Storch-Bergmann, T., Riffel, R. A., et al. 2006, *ApJ*, 641, L25
- Fathi, K., van de Ven, G., Peletier, R. F., et al. 2005, *MNRAS*, 364, 773
- Finkelman, I., Moiseev, A., Brosch, N., & Katkov, I. 2011, *MNRAS*, 418, 1834
- Franx, M., van Gorkom, J. H., & de Zeeuw, T. 1994, *ApJ*, 436, 642
- Fridman, A. M., Afanasiev, V. L., Dodonov, S. N., et al. 2005, *A&A*, 430, 67
- Fridman, A. M., Khoruzhii, O. V., Lyakhovich, V. V., et al. 2001a, *A&A*, 371, 538
- Fridman, A. M., Khoruzhii, O. V., Polyachenko, E. V., et al. 2001b, *MNRAS*, 323, 651
- Fridman, A. M., Koruzhii, O. V., Zasov, A. V., et al. 1998, *Astronomy Letters*, 24, 764
- Fridman, A. M., Morozov, A. G., Nezhlin, M. V., & Snezhkin, E. N. 1985, *Physics Letters A*, 109, 228
- Gebhardt, K., Pryor, C., O’Connell, R. D., Williams, T. B., & Hesser, J. E. 2000, *AJ*, 119, 1268
- Gebhardt, K., Pryor, C., Williams, T. B., & Hesser, J. E. 1995, *AJ*, 110, 1699
- González, J. J., Cepa, J., González-Serrano, J. I., & Sánchez-Portal, M. 2014, *MNRAS*, 443, 3289
- Gordon, S., Koribalski, B., Houghton, S., & Jones, K. 2000, *MNRAS*, 315, 248
- Haffner, L. M., Reynolds, R. J., Tufte, S. L., et al. 2003, *ApJS*, 149, 405
- Hagen-Thorn, V. A., Shalyapina, L. V., Karataeva, G. M., et al. 2005, *Astronomy Reports*, 49, 958
- Hernandez, O., Fathi, K., Carignan, C., et al. 2008, *PASP*, 120, 665
- Jeanneau, A., Kosmalski, J., Muslimov, E., et al. 2020, in *Society of Photo-Optical Instrumentation Engineers (SPIE) Conference Series*, Vol. 11447, *Society of Photo-Optical Instrumentation Engineers (SPIE) Conference Series*, 114475M
- Józsa, G. I. G., Kenn, F., Klein, U., & Oosterloo, T. A. 2007, *A&A*, 468, 731
- Keel, W. C., Lintott, C. J., Maksym, W. P., et al. 2017, *ApJ*, 835, 256
- Keel, W. C., Maksym, W. P., Bennert, V. N., et al. 2015, *AJ*, 149, 155
- Kelz, A., Verheijen, M. A. W., Roth, M. M., et al. 2006, *PASP*, 118, 129
- Kentischer, T. J., Schmidt, W., Sigwarth, M., & Uexkuell, M. V. 1998, *A&A*, 340, 569
- Khoperskov, S., Moiseev, A., & Khoperskov, A. 2013, *Memorie della Societa Astronomica Italiana Supplementi*, 25, 51
- Khoperskov, S. A., Moiseev, A. V., Khoperskov, A. V., & Saburova, A. S. 2014, *MNRAS*, 441, 2650
- Kozlova, D. V., Moiseev, A. V., & Smirnova, A. A. 2020, *Contributions of the Astronomical Observatory Skalnat Pleso*, 50, 309
- Krajnović, D., Cappellari, M., de Zeeuw, P. T., & Copin, Y. 2006, *MNRAS*, 366, 787
- Kraus, M., Liimets, T., Moiseev, A., et al. 2021, *AJ* accepted, arXiv:2106.15981
- Krumholz, M. R., Burkhardt, B., Forbes, J. C., & Crocker, R. M. 2018, *MNRAS*, 477, 2716
- Lintott, C. J., Schawinski, K., Keel, W., et al. 2009, *MNRAS*, 399, 129
- López-Cobá, C., Sánchez, S. F., Bland-Hawthorn, J., et al. 2019, *MNRAS*, 482, 4032
- López-Cobá, C., Sánchez, S. F., Moiseev, A. V., et al. 2017, *MNRAS*, 467, 4951
- Lozinskaya, T. A. 1969, *Soviet Ast.*, 13, 192
- Lozinskaya, T. A. 1973, *Soviet Ast.*, 16, 945
- Lozinskaya, T. A., Komarova, V. N., Moiseev, A. V., & Blinnikov, S. I. 2005, *Astronomy Letters*, 31, 245
- Lozinskaya, T. A. & Moiseev, A. V. 2007, *MNRAS*, 381, L26
- Lozinskaya, T. A., Moiseev, A. V., & Podorvanyuk, N. Y. 2003, *Astronomy Letters*, 29, 77
- Lyakhovich, V. V., Fridman, A. M., Khoruzhii, O. V., & Pavlov, A. I. 1997, *Astronomy Reports*, 41, 447
- Marcelin, M., Amram, P., Balard, P., et al. 2008, in *Society of Photo-Optical Instrumentation Engineers (SPIE) Conference Series*, Vol. 7014, *Ground-based and Airborne Instrumentation for Astronomy II*, ed. I. S. McLean & M. M. Casali, 701455
- Marcelin, M., Boulesteix, J., & Courtes, G. 1982, *A&A*, 108, 134
- Marcelin, M., Boulesteix, J., & Georgelin, Y. 1983, *A&A*, 128, 140
- Martínez-Delgado, D., Gabany, R. J., Crawford, K., et al. 2010, *AJ*, 140, 962
- Martínez-Delgado, I., Tenorio-Tagle, G., Muñoz-Tuñón, C., Moiseev, A. V., & Cairós, L. M. 2007, *AJ*, 133, 2892
- Melnick, J., Moles, M., Terlevich, R., & García-Pelayo, J.-M. 1987, *MNRAS*, 226, 849
- Mendes de Oliveira, C., Amram, P., Quint, B. C., et al. 2017, *MNRAS*, 469, 3424
- Merkulova, O. A., Karataeva, G. M., Yakovleva, V. A., & Burenkov, A. N. 2012, *Astronomy Letters*, 38, 290
- Merkulova, O. A., Shalyapina, L. V., & Yakovleva, V. A. 2009, *Astronomy Letters*, 35, 587
- Mitchell, C. J., Williams, T. B., Spekkens, K., et al. 2015, *AJ*, 149, 116
- Moiseev, A. 2011, in *EAS Publications Series*, Vol. 48, *EAS Publications Series*, ed. M. Koleva, P. Prugniel, & I. Vauglin, 115–118
- Moiseev, A. 2014a, in *Astronomical Society of the Pacific Conference Series*, Vol. 486, *Multi-Spin Galaxies*, ed. E. Iodice & E. M. Corsini, 61
- Moiseev, A., Khoperskov, S., Khoperskov, A., et al. 2015a, *Baltic Astronomy*, 24, 76
- Moiseev, A., Perepelitsyn, A., & Oparin, D. 2020, *Experimental Astronomy*, 50, 199
- Moiseev, A. V. 2000, *A&A*, 363, 843
- Moiseev, A. V. 2002, *Bulletin of the Special Astrophysics Observatory*, 54, 74

- Moiseev, A. V. 2008, *Astrophysical Bulletin*, 63, 201
- Moiseev, A. V. 2012, *Astrophysical Bulletin*, 67, 147
- Moiseev, A. V. 2014b, *Astrophysical Bulletin*, 69, 1
- Moiseev, A. V. 2015, *Astrophysical Bulletin*, 70, 494
- Moiseev, A. V. & Bizyaev, D. V. 2009, *New Astronomy Reviews*, 53, 169
- Moiseev, A. V. & Egorov, O. V. 2008, *Astrophysical Bulletin*, 63, 181
- Moiseev, A. V. & Lozinskaya, T. A. 2012, *MNRAS*, 423, 1831
- Moiseev, A. V. & Mustsevoi, V. V. 2000, *Astronomy Letters*, 26, 565
- Moiseev, A. V., Pustilnik, S. A., & Kniazev, A. Y. 2010, *MNRAS*, 405, 2453
- Moiseev, A. V., Smirnova, K. I., Smirnova, A. A., & Reshetnikov, V. P. 2011, *MNRAS*, 418, 244
- Moiseev, A. V., Tikhonov, A. V., & Klypin, A. 2015b, *MNRAS*, 449, 3568
- Moiseev, A. V., Valdés, J. R., & Chavushyan, V. H. 2004, *A&A*, 421, 433
- Monnet, G. 1995, in *Astronomical Society of the Pacific Conference Series*, Vol. 71, IAU Colloq. 149: Tridimensional Optical Spectroscopic Methods in Astrophysics, ed. G. Comte & M. Marcellin, 12
- Morgenthaler, J. P., Harris, W. M., Scherb, F., et al. 2001, *ApJ*, 563, 451
- Morozov, A. G. 1979, *AZh*, 56, 498
- Morrissey, P., Matuszewski, M., Martin, D. C., et al. 2018, *ApJ*, 864, 93
- Movsessian, T. A., Magakian, T. Y., Bally, J., et al. 2007, *A&A*, 470, 605
- Movsessian, T. A., Magakian, T. Y., & Burenkov, A. N. 2019, *A&A*, 627, A94
- Movsessian, T. A., Magakian, T. Y., & Moiseev, A. V. 2012, *A&A*, 541, A16
- Munoz-Tunon, C., Tenorio-Tagle, G., Castaneda, H. O., & Terlevich, R. 1996, *AJ*, 112, 1636
- Oparin, D. V. & Moiseev, A. V. 2015, *Astrophysical Bulletin*, 70, 392
- Oparin, D. V. & Moiseev, A. V. 2018, *Astrophysical Bulletin*, 73, 298
- Plana, H. & Boulesteix, J. 1996, *A&A*, 307, 391
- Plana, H., Boulesteix, J., Amram, P., Carignan, C., & Mendes de Oliveira, C. 1998, *A&AS*, 128, 75
- Poutanen, J., Fabrika, S., Valeev, A. F., Sholukhova, O., & Greiner, J. 2013, *MNRAS*, 432, 506
- Punzo, D., van der Hulst, J. M., Roerdink, J. B. T. M., et al. 2015, *Astronomy and Computing*, 12, 86
- Pustilnik, S. A., Makarova, L. N., Perepelitsyna, Y. A., Moiseev, A. V., & Makarov, D. I. 2017, *MNRAS*, 465, 4985
- Ramya, S., Sahu, D. K., & Prabhu, T. P. 2007, *MNRAS*, 381, 511
- Rangwala, N., Williams, T. B., Pietraszewski, C., & Joseph, C. L. 2008, *AJ*, 135, 1825
- Rangwala, N., Williams, T. B., & Stanek, K. Z. 2009, *ApJ*, 691, 1387
- Rogstad, D. H., Lockhart, I. A., & Wright, M. C. H. 1974, *ApJ*, 193, 309
- Rosado, M., Langerica, R., Bernal, A., et al. 1995, in *Revista Mexicana de Astronomia y Astrofisica Conference Series*, Vol. 3, *Revista Mexicana de Astronomia y Astrofisica Conference Series*, ed. M. Pena & S. Kurtz, 263
- Roy, J. R., Arsenault, R., & Joncas, G. 1986, *ApJ*, 300, 624
- Ryder, S. D., Zasov, A. V., McIntyre, V. J., Walsh, W., & Sil'chenko, O. K. 1998, *MNRAS*, 293, 411
- Sakhibov, F. K. & Smirnov, M. A. 1989, *Soviet Ast.*, 33, 476
- Shalyapina, L. V., Merkulova, O. A., Yakovleva, V. A., & Volkov, E. V. 2007, *Astronomy Letters*, 33, 520
- Shalyapina, L. V., Moiseev, A. V., Yakovleva, V. A., Hagen-Thorn, V. A., & Barsunova, O. Y. 2004a, *Astronomy Letters*, 30, 583
- Shalyapina, L. V., Moiseev, A. V., Yakovleva, V. A., Hagen-Thorn, V. A., & Burenkov, A. N. 2004b, *Astronomy Letters*, 30, 1
- Sheglov, P. V. 1963, *Nature*, 199, 990
- Sil'chenko, O. K. & Moiseev, A. V. 2006, *AJ*, 131, 1336
- Sil'chenko, O. K., Moiseev, A. V., & Egorov, O. V. 2019, *ApJS*, 244, 6
- Sitnik, T. G., Egorov, O. V., Lozinskaya, T. A., et al. 2019, *MNRAS*, 486, 2449
- Smirnova, A. & Moiseev, A. 2010, *MNRAS*, 401, 307
- Smirnova, A. A., Gavrilović, N., Moiseev, A. V., et al. 2007, *MNRAS*, 377, 480
- Smirnova, A. A., Moiseev, A. V., & Afanasiev, V. L. 2006, *Astronomy Letters*, 32, 520
- Smirnova, A. A., Moiseev, A. V., & Dodonov, S. N. 2018, *MNRAS*, 481, 4542
- Soto, K. T., Lilly, S. J., Bacon, R., Richard, J., & Conseil, S. 2016, *MNRAS*, 458, 3210
- Streicher, O., Weibacher, P. M., Bacon, R., & Jarno, A. 2011, in *Astronomical Society of the Pacific Conference Series*, Vol. 442, *Astronomical Data Analysis Software and Systems XX*, ed. I. N. Evans, A. Accomazzi, D. J. Mink, & A. H. Rots, 257
- Taylor, K. & Atherton, P. D. 1980, *MNRAS*, 191, 675
- Teuben, P. J. 2002, in *Astronomical Society of the Pacific Conference Series*, Vol. 275, *Disks of Galaxies: Kinematics, Dynamics and Perturbations*, ed. E. Athanassoula, A. Bosma, & R. Mújica, 217–228
- Tully, R. B. 1974, *ApJS*, 27, 415
- Veilleux, S., Weiner, B. J., Rupke, D. S. N., et al. 2010, *AJ*, 139, 145
- Weitzel, L., Krabbe, A., Kroker, H., et al. 1996, *A&AS*, 119, 531
- Whitmore, B. C., Lucas, R. A., McElroy, D. B., et al. 1990, *AJ*, 100, 1489
- Yakovleva, V. A., Merkulova, O. A., Karataeva, G. M., et al. 2016, *Astronomy Letters*, 42, 215
- Yang, H., Chu, Y.-H., Skillman, E. D., & Terlevich, R. 1996, *AJ*, 112, 146
- Zasov, A. V. & Moiseev, A. V. 1999, in *Activity in Galaxies and Related Phenomena*, ed. Y. Terzian,

- E. Khachikian, & D. Weedman, Vol. 194, 279
- Zasov, A. V. & Sil'chenko, O. K. 1996, in *Astronomical Society of the Pacific Conference Series*, Vol. 91, IAU Colloq. 157: Barred Galaxies, ed. R. Buta, D. A. Crocker, & B. G. Elmegreen, 207

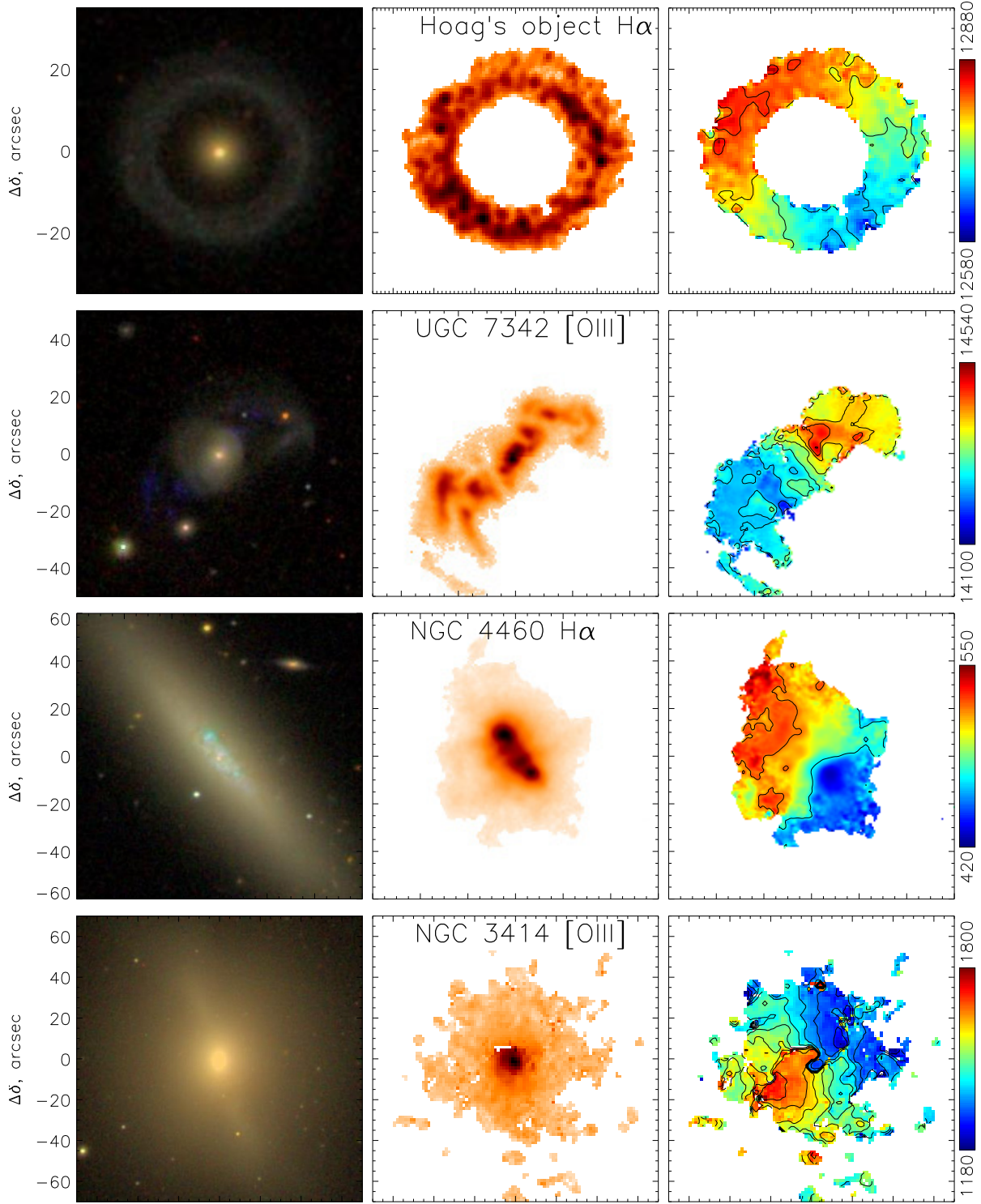


Fig. 6. Galaxies with gas kinematics dominated by circular rotation. Left to right: image from SDSS, brightness distribution in the emission line labeled and the velocity field derived from FPI observations made on the 6-m telescope. The scale is in km s^{-1} . Top to bottom: Hoag’s object (Finkelman et al., 2011), the active galaxy UGC 7342 (Keel et al., 2015), galactic wind in NGC 4460 (Oparin & Moiseev, 2015), and the inner polar disk in the lenticular galaxy NGC 3414 (Sil’chenko et al., 2019).

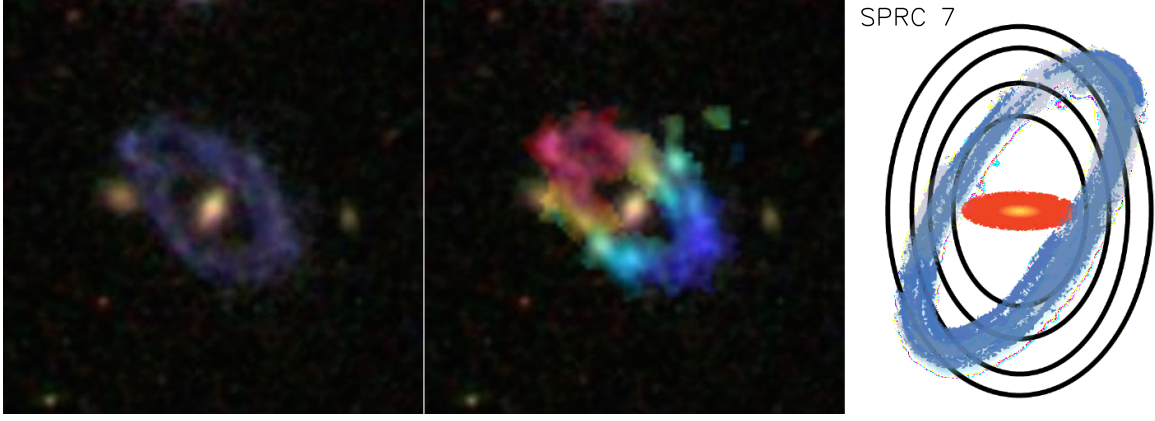


Fig. 7. Polar ring in SPRC-7. Left to right: color image from SDSS; matching SDSS data with the velocity field inferred from FPI data, the colors are used to code observed line-of-sight velocities and intensity in accordance with the $H\beta$ emission-line brightness distribution; the distribution of the gravitational potential of the dark-matter halo is adopted in accordance with numerical computations. Shown schematically are the central disk and the polar (tilted) ring (Moiseev et al., 2015a).

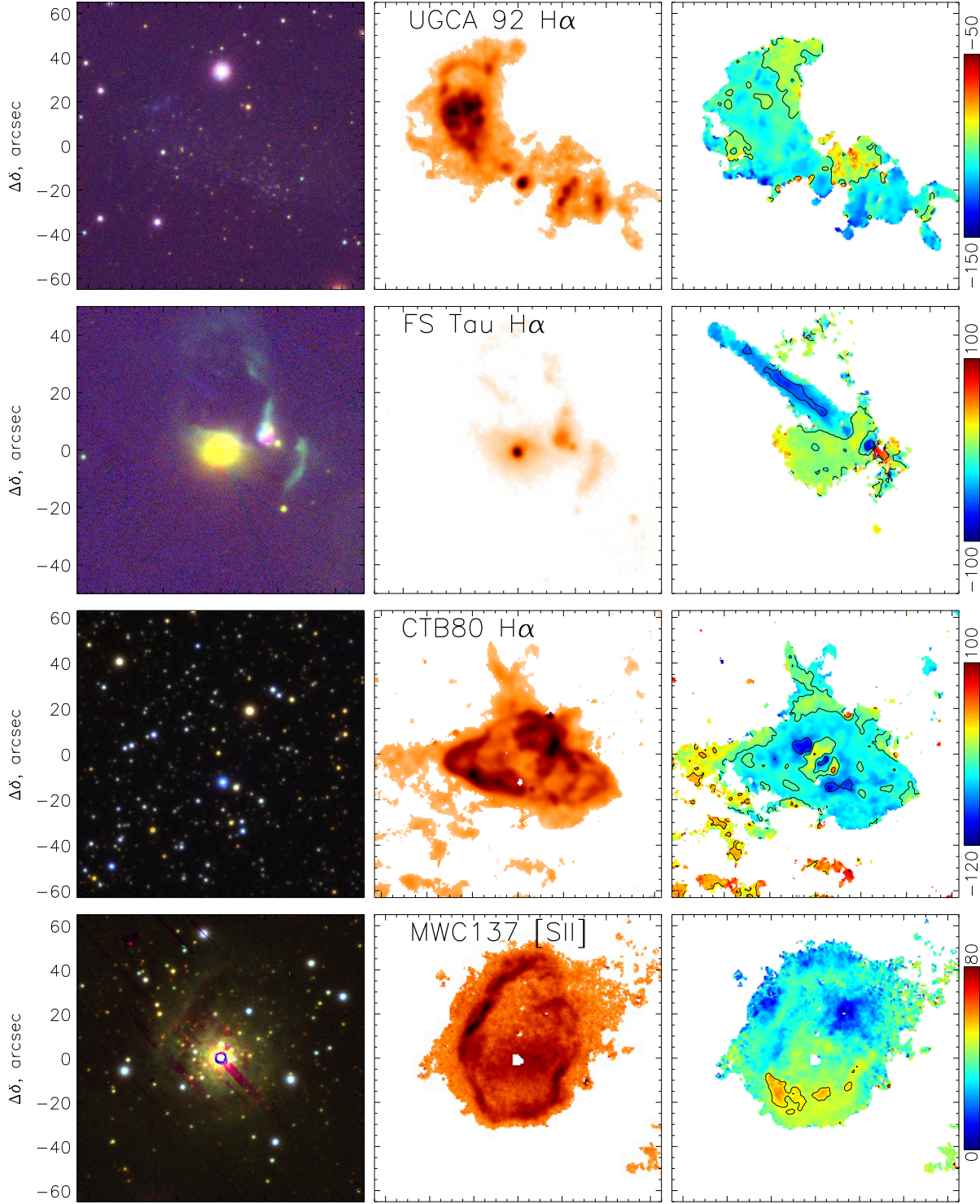


Fig. 8. Objects with appreciable influence of stars on the gaseous medium. Left to right: Pan-STARRS DR1 image of the brightness distribution in the emission line labeled and the velocity field of ionized gas based on FPI observations performed on the 6-m telescope. Top to bottom: the dwarf galaxy UGC 92 (Moiseev et al., 2015b); a jet in the vicinity of the young star FS Tau (Movsessian et al., 2019); the pulsar nebula CTB 80 (Lozinskaya et al., 2005), and the nebula surrounding the Be star MWC 137 (Kraus et al., 2021).

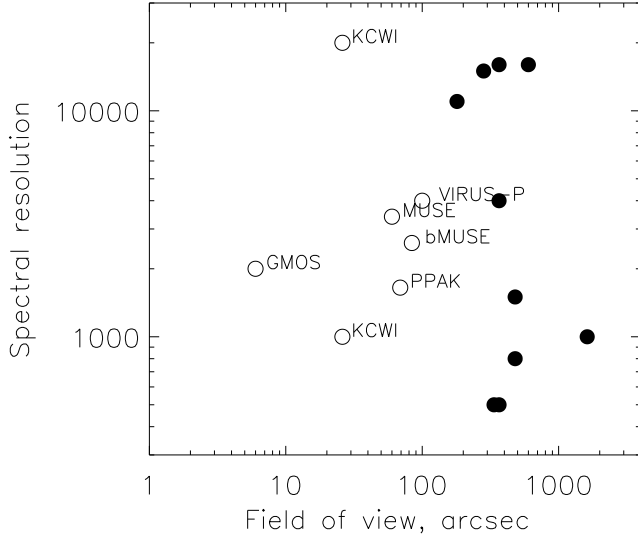


Fig. 9. Parameters of instruments for 3D spectroscopy based on scanning FPIs (the black dots) and integral-field spectrographs (open circles) in the “FOV– \mathcal{R} ” plane. For KCWI the modes of high and low spectral resolution are shown.